

International Journal of Modern Physics E
 © World Scientific Publishing Company

Viscous Hydrodynamics and the Quark Gluon Plasma

Derek A. Teaney

*Department of Physics and Astronomy, Stony Brook University,
 Stony Brook, New York 11794-3800, United States
 derek.teaney@stonybrook.edu*

Received November 26, 2024

One of the most striking results from the Relativistic Heavy Ion Collider is the strong elliptic flow. This review summarizes what is observed and how these results are combined with reasonable theoretical assumptions to estimate the shear viscosity of QCD near the phase transition. A data comparison with viscous hydrodynamics and kinetic theory calculations indicates that the shear viscosity to entropy ratio is surprisingly small, $\eta/s < 0.4$. The preferred range is $\eta/s \simeq (1 \leftrightarrow 3) \times 1/4\pi$.

1. Introduction

One of the most striking observations from the Relativistic Heavy Ion Collider (RHIC) is the very large elliptic flow^{1,2}. The primary goal of this report is to explain as succinctly as possible precisely what is observed and how the shear viscosity can be estimated from these observations. The resulting estimates^{3,4,5,6,7,8,9,10,11,12} indicate that the shear viscosity to entropy ratio η/s is close to the limits suggested by the uncertainty principle¹³, and the result of $\mathcal{N} = 4$ Super Yang Mills (SYM) theory at strong coupling^{14,15}

$$\frac{\eta}{s} = \frac{1}{4\pi}.$$

These estimates imply that the heavy ion experiments are probing quantum kinetic processes in this theoretically interesting, but poorly understood regime. Clearly a complete understanding of nucleus-nucleus collisions at high energies is extraordinarily difficult. We will attempt to explain the theoretical basis for these recent claims and the uncertainties in the estimated values of η/s . Additionally, since the result has raised considerable interest outside of the heavy ion community, this review will try to make the analysis accessible to a fairly broad theoretical audience.

1.1. *Experimental Overview*

In high energy nucleus-nucleus collisions at RHIC approximately ~ 7000 particles are produced in a single gold-gold event with collision energy, $\sqrt{s} = 200$ GeV/nucleon. Each nucleus has 197 nucleons and the two nuclei are initially

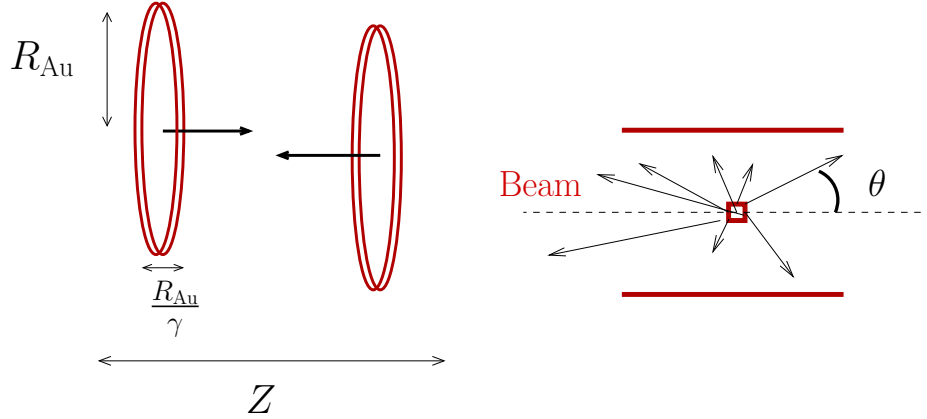
2 *Derek A. Teaney*

Fig. 1. Overview of a heavy ion event. In the left figure the two nuclei collide along the beam axis usually labeled as Z . At RHIC the nuclei are length contracted by a factor of $\gamma \simeq 100$. The right figure shows the collision vertex of a typical event as viewed in a schematic particle detector and shows a few of the thousands of charged particle tracks recorded per event. The angle θ is usually reported in pseudo-rapidity variables as discussed in the text.

length contracted by a factor of a hundred. The transverse size of the nucleus is $R_{\text{Au}} \sim 5$ fm and the duration of the event is roughly of order $\sim R_{\text{Au}}/c$. Fig. 1 shows the pre-collision geometry. Also shown is a schematic of the collision vertex and a schematic particle detector.

Usually the two nuclei collide off-center at impact parameter \mathbf{b} and oriented at an angle Ψ_{RP} with respect to the lab axes as shown in Fig. 2. During the collision the spectator nucleons (see Fig. 2) continue down the beam pipe, leaving behind an excited almond shaped region. The impact parameter \mathbf{b} is a transverse vector $\mathbf{b} = (b_x, b_y)$ pointing from the center of one nucleus to the center of the other. As discussed in Section 2 both the magnitude and direction of \mathbf{b} can be determined on an event by event basis. We will generally work with reaction plane coordinates X and Y rather than lab coordinates.

The elliptic flow is defined as the anisotropy of particle production with respect to the reaction plane (see Fig. 2 and Fig. 3)

$$v_2 \equiv \left\langle \frac{p_X^2 - p_Y^2}{p_X^2 + p_Y^2} \right\rangle, \quad (1)$$

or the second Fourier coefficient of the azimuthal distribution, $\langle \cos(2(\phi - \Psi_{RP})) \rangle$. Elliptic flow can also be measured as a function of transverse momentum $p_T = \sqrt{p_X^2 + p_Y^2}$ by expanding the differential yield of particles in a Fourier series

$$\frac{1}{p_T} \frac{dN}{dy dp_T d\phi} = \frac{1}{2\pi p_T} \frac{dN}{dy dp_T} (1 + 2v_2(p_T) \cos 2(\phi - \Psi_{RP}) + \dots). \quad (2)$$

Here ellipses denote still higher harmonics, v_4 , v_6 and so on. In addition the flow can be measured as a function of impact parameter, particle type, and rapidity. For

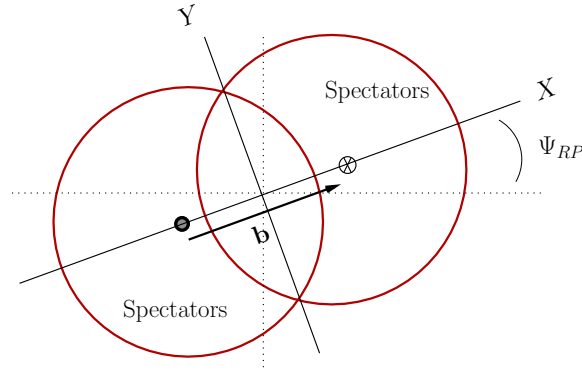


Fig. 2. A schematic of the transverse plane in a heavy ion event. Both the magnitude and direction of the impact parameter \mathbf{b} can be determined on an event by event basis. X and Y label the reaction plane axes and the dotted lines indicate the lab axis. Ψ_{RP} is known as the reaction plane angle.

a mid-peripheral collision ($b \simeq 7$ fm) the average elliptic flow $\langle v_2 \rangle$ is approximately 7%. This is surprising large. For instance, the ratio of particles in the X direction to the Y is $1 + 2v_2 : 1 - 2v_2 \simeq 1.3 : 1$. At higher transverse momentum the elliptic flow grows and at $p_T \sim 1.5$ GeV elliptic flow can be as large as 15%.

1.2. An Interpretation of Elliptic Flow

The generally accepted explanation for the observed flow is illustrated in Fig. 3. Since the pressure gradient in the X direction is larger than in the Y direction, the nuclear medium expands preferentially along the short axis of the ellipse. Elliptic flow is such a useful observable because it is a rather direct probe of the response of the QCD medium to the high energy density created during the event. If the mean free path is large compared to the size of the interaction region, then the produced particles will not respond to the initial geometry. On the other hand, if the transverse size of the nucleus is large compared to the interaction length scales involved, hydrodynamics is the appropriate theoretical framework to calculate the response of the medium to the geometry. In a pioneering paper by Ollitrualt, the elliptic flow observable was proposed and analyzed based partly on the conviction that ideal hydrodynamic models would vastly over-predict the flow^{16,17}.

However, calculations based on ideal hydrodynamics do a fair to reasonable job in reproducing the observed elliptic flow^{18,19,20,21,22}. This has been reviewed elsewhere^{23,24}. Nevertheless, the hydrodynamic interpretation requires that the relevant mean free paths and relaxation times be small compared to the nuclear sizes and expansion rates. This review will assess the consistency of the hydrodynamic interpretation by categorizing viscous corrections. The principle tool is viscous hydrodynamics which needs to be extended into the relativistic domain

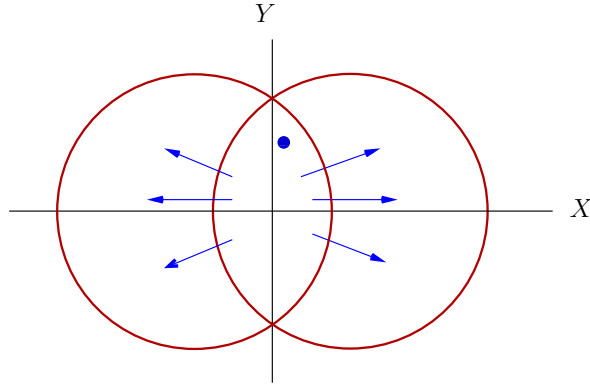
4 *Derek A. Teaney*

Fig. 3. The conventional explanation for the observed elliptic flow. The spectators continue down the beam pipe leaving behind an excited oval shape which expands preferentially along the short axis of the ellipse. The final momentum asymmetry in the particle distribution v_2 reflects the response of the excited medium to this geometry. The dot with transverse coordinate $\mathbf{x} = (x, y)$ is illustrated to explain a technical point in Section 2.

in order to address the problems associated with nuclear collisions. This problem has received considerable attention recently and progress has been achieved both at a conceptual ^{25,26,27,28,29} and practical level ^{5,9,30,10,31,11}. Generally macroscopic approaches, such as viscous hydrodynamics, and microscopic approaches, such as kinetic theory, are converging on the implications of the measured elliptic flow ^{29,32,12,33,6,34}. There has never been an even remotely successful model of the flow with $\eta/s > 0.4$. Since η/s is a measure of the relaxation time relative to $\hbar/k_B T$ (see Section 3), this estimate of η/s places the kinetic processes measured at RHIC in an interesting and fully quantum regime.

2. Elliptic Flow – Measurements and Definitions

The goal of this section is to review the progress that has been achieved in measuring the elliptic flow. This progress has produced an increasingly self-consistent hydrodynamic interpretation of the observed elliptic flow results. This section will also collect the various definitions which are needed to categorize the response of the excited medium to the initial geometry.

2.1. Measurements and Definitions

As discussed in the introduction (see Fig. 2) both the magnitude and direction of the impact parameter can be determined on an event by event basis. The magnitude of the impact parameter can be determined by selecting events with definite multiplicity for example. For instance, on average the top 10% of events with the highest multiplicity correspond to the 10% of events with the smallest impact parameter. Since the cross section is almost purely geometrical in this energy range

this top 10% of events may be found by a purely geometrical argument. This line of reasoning gives that the top 10% of events are produced by collisions with an impact parameter in the range

$$0 < b < b_*, \quad \text{where} \quad 10\% = \frac{\pi b_*^2}{\sigma_{\text{tot}}}, \quad (3)$$

and $\sigma_{\text{tot}} \simeq \pi(2R_A)^2$ is the total inelastic cross section. After categorizing the top 10% of events we can categorize the top 10-20% of events and so on. The general relation is

$$\left(\frac{b}{2R_A}\right)^2 \simeq \% \text{ Centrality}. \quad (4)$$

Here we have neglected fluctuations and many other effects. For instance there is a very small probability that an event with impact parameter $b = 4$ fm will produce the same multiplicity as an event with $b = 0$ fm. A full discussion of these and many other issues is given in Ref.³⁵. The end result is that the magnitude of the impact parameter \mathbf{b} can be determined to within half a femtometer or so³⁶.

Now that the impact parameter is quantified, a useful definition is the number of participating nucleons (also called “wounded” nucleons). The number of nucleons per unit volume in the rest frame of the nucleus is $\rho_A(\mathbf{x} - \mathbf{x}_o, z)$, where $\mathbf{x} - \mathbf{x}_o$ is the transverse displacement from a nucleus centered at \mathbf{x}_o , and z is the longitudinal direction. These distributions are known experimentally and are reasonably modeled by a Woods-Saxon form³⁵. The number of nucleons per unit transverse area is

$$T_A(\mathbf{x} - \mathbf{x}_o) = \int_{-\infty}^{\infty} dz \rho_A(\mathbf{x} - \mathbf{x}_o, z). \quad (5)$$

Then, after reexamining Fig. 3, we find that the probability that a nucleon at $\mathbf{x} = (x, y)$ will suffer an inelastic interaction passing through the right nucleus centered $\mathbf{b}/2 = (+b/2, 0)$ is

$$1 - \exp(-\sigma_{\text{NN}} T_A(\mathbf{x} - \mathbf{b}/2)),$$

where $\sigma_{\text{NN}} \simeq 40$ mb is the inelastic nucleon-nucleon cross section. The number of nucleons which suffer an inelastic collision per unit area is then

$$\begin{aligned} \frac{dN_p}{dx dy} &= T_A(\mathbf{x}_\perp + \mathbf{b}/2) [1 - \exp(-\sigma_{\text{NN}} T_A(\mathbf{x}_\perp - \mathbf{b}/2))] \\ &\quad + T_A(\mathbf{x}_\perp - \mathbf{b}/2) [1 - \exp(-\sigma_{\text{NN}} T_A(\mathbf{x}_\perp + \mathbf{b}/2))] . \end{aligned} \quad (6)$$

Finally, the total number of participants (*i.e.* the the number of nucleons which collide) is

$$N_p = \int dx dy \frac{dN}{dx dy}. \quad (7)$$

For a central collision of two gold nuclei the number of participants $N_p \simeq 340$ nearly equals the total number nucleons in the two nuclei, $N = 394$, leaving about fifty

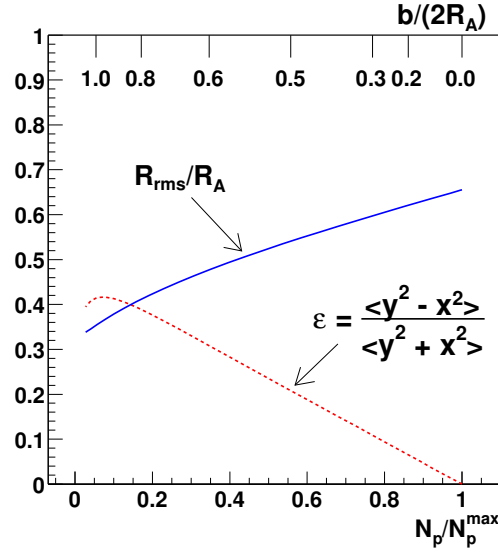
6 *Derek A. Teaney*

Fig. 4. The standard Glauber eccentricity $\epsilon_{s,\text{part}}$ as a function of the number of participants. $N_p^{\text{max}} \simeq 340$ is the maximum number of participants in a central AuAu event and $R_A \simeq 6.3$ fm is the gold radius. The top axis shows the translation between impact parameter and participants. The root mean square radius R_{rms} and the standard Glauber eccentricity are given in Eq. (13) and Eq. (15).

spectators. By comparing the top axis in Fig. 4 to the bottom axis, the relationship between participants, impact parameter b , and centrality can be determined.

The reaction plane angle, Ψ_{RP} , is also determined experimentally. Here we will describe the Event Plane method which is conceptually the simplest. Assume first that the reaction plane angle is known. Then the particle distribution can be expanded in harmonics about the reaction plane

$$\frac{dN}{d\phi} \propto 1 + 2v_2 \cos(2(\phi - \Psi_{RP})) + \dots \quad (8)$$

If the number of particles is very large one could simply make a histogram of the angular distribution of particles in an event with respect to the lab axis. Then the reaction plane angle could be determined by finding where the histogram is maximum. This is the basis of the event plane method³⁷. For all the particles in the event we form the vector

$$\vec{Q} = (Q_x, Q_y) = \left(\sum_i \cos 2\phi_i, \sum_i \sin 2\phi_i \right). \quad (9)$$

Using the continuum approximation, $Q_x \simeq \int d\phi dN/d\phi \cos(2\phi)$, we can estimate

the reaction plane angle Ψ_{RP} , from the \vec{Q} -vector

$$\frac{\vec{Q}}{|\vec{Q}|} \equiv (\cos(2\Psi_2), \sin(2\Psi_2)) \simeq (\cos(2\Psi_{RP}), \sin(2\Psi_{RP})) . \quad (10)$$

Then we can estimate the elliptic flow as $v_2^{\text{obs}} \simeq \langle \cos(2(\phi_i - \Psi_2)) \rangle$. The estimated angle Ψ_2 differs from Ψ_{RP} due to statistical fluctuations. Consequently v_2^{obs} will be systematically smaller than v_2 since Ψ_2 is not Ψ_{RP} . This leads to a correction to the estimate given above which is known as the reaction plane resolution. The final result, after considering the dispersion of Ψ_2 relative to the true reaction plane angle Ψ_{RP} is

$$v_2 = \frac{v_2^{\text{obs}}}{\mathcal{R}} \quad \text{where} \quad \mathcal{R} = \langle \cos 2(\Psi_2 - \Psi_{RP}) \rangle . \quad (11)$$

In practice the resolution parameter \mathcal{R} is estimated by dividing a given event into sub-events and looking at the dispersion in Ψ_2 between different sub-events.

There is *a lot* more to the determination of the event plane in practice. Fortunately the various methods have been reviewed recently³⁷. An important criterion for the validity of these methods is that the magnitude of elliptic flow be large compared to statistical fluctuations

$$v_2^2 \gg \frac{1}{N} . \quad (12)$$

For $v_2 \simeq 7\%$ and $N \simeq 500$ we have $Nv_2^2 \simeq 2.5$. Since this number is not particularly large the simple method described above is not completely adequate in practice. The resolution parameter is $\mathcal{R} \simeq 0.7$ in the STAR experiment. At the LHC, estimates suggest that the resolution parameter \mathcal{R} could be as large as³⁸ $\mathcal{R} \simeq 0.95$. Current methods use two particle, four particle, and higher cumulants to remove the effects of correlations and fluctuations. These advances are discussed more completely in Section 2.3 and have played an important role in the current estimates of the shear viscosity. The current measurements provide a unique theoretical opportunity to study systematically how hydrodynamics begins to develop in mesoscopic systems.

We would like to measure the response of nuclei to the geometry. To this end, we categorize the overlap region with an asymmetry parameter $\epsilon_{s,\text{part}}$

$$\epsilon_{s,\text{part}} = \frac{\langle y^2 - x^2 \rangle}{\langle y^2 + x^2 \rangle} . \quad (13)$$

Traditionally the average $\langle \dots \rangle$ is taken with respect to the number of participants in the transverse plane, for example

$$\langle y^2 - x^2 \rangle = \frac{1}{N_p} \int dx dy (y^2 - x^2) \frac{dN_p}{dx dy} . \quad (14)$$

We will explain the “s,part” label shortly; for the moment we return to Fig. 4, which plots the asymmetry parameter versus centrality and also shows the the root mean square radius

$$R_{\text{rms}} = \sqrt{\langle x^2 + y^2 \rangle} , \quad (15)$$

which is important for categorizing the size of viscous corrections.

2.2. Interpretation

We have collected the essential definitions of ϵ , centrality, and v_2 , and are now in a position to return to the physics. The scaled elliptic flow v_2/ϵ measures the response of the medium to the initial geometry. Fig. 5 shows $v_2(p_T)/\epsilon$ as a function of centrality, 0-5% being the most central and 60-70% being the most peripheral. Examining this figure we see a gradual transition from a weak to a strong dynamic response with growing system size. The interpretation adopted in this review is that this change is a consequence of a system transitioning from a kinetic to a hydrodynamic regime.

There are several theoretical curves based upon calculations of ideal hydrodynamics^{21,20} which for $p_T < 1$ GeV approximately reproduce the observed elliptic flow in the most central collisions. Since ideal hydrodynamics is scale invariant (for a scale invariant equation of state) the expectation is that the response v_2/ϵ of this theory should be independent of system size or centrality. This reasoning is borne out by the more elaborate hydrodynamic calculations shown in the figure. On the other hand, the data show a gradual transition as a function of increasing centrality, rising towards the ideal hydrodynamic calculations in a systematic way. These trends are captured by models with a finite mean free path⁴¹.

The data show other trends as a function of centrality. In more central collisions the linearly rising trend, which resembles the ideal hydrodynamic calculations, extends to larger and larger transverse momentum. We will see in Section 5 that viscous corrections to ideal hydrodynamics grow as

$$\left(\frac{p_T}{T}\right)^2 \frac{\ell_{\text{mfp}}}{L}, \quad (16)$$

where L is a characteristic length scale. Thus these viscous corrections restrict the applicable momentum range in hydrodynamics⁴. In more central collisions, where ℓ_{mfp}/L is smaller, the transverse momentum range described by hydrodynamics extends to increasingly large p_T . These qualitative trends are reproduced by the more involved viscous calculations discussed in Section 6.

To conclude this section, we turn to Fig. 6 which compares the elliptic protons and pions to the flow of the multi-strange hadrons Ω^- and ϕ . (These hadrons have valence quark content sss and $s\bar{s}$ respectively.) The important point is that the Ω^- is nearly twice as heavy as the proton and more importantly, does not have a strong resonant interaction analogous to the Δ . For these reasons the hadronic relaxation time of the Ω^- is expected to be much longer than the duration of the heavy ion event⁴². Nevertheless the Ω shows nearly the same elliptic flow as the protons. This provides fairly convincing evidence that the majority of the elliptic flow develops during a deconfined phase which hadronizes to produce a flowing Ω^- baryon.

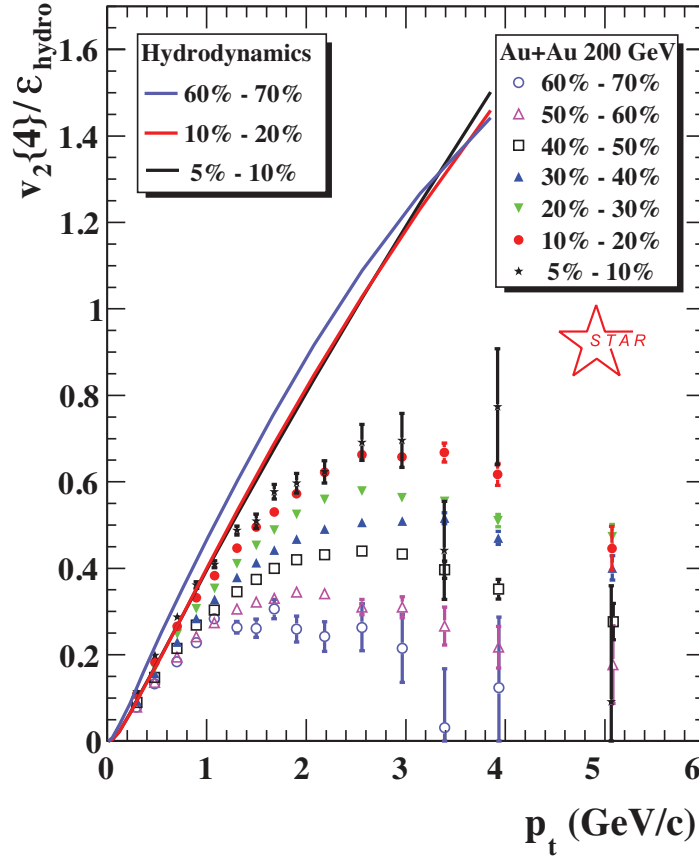


Fig. 5. Elliptic flow $v_2(p_T)$ as measured by the STAR collaboration^{39,40} for different centralities. The measured elliptic flow has been divided by the eccentricity – $\epsilon_{\text{hydro}} \equiv \epsilon_{s,\text{part}}$ in this work. The curves are ideal hydrodynamic calculations based on Refs.^{23,21} rather than the viscous hydrodynamics discussed in much of this review.

2.3. The Eccentricity and Fluctuations

Clearly much of the interpretation of elliptic flow relies on a solid understanding of the eccentricity. There are several issues here. First there is the theoretical uncertainty in this average quantity. For example, so far we have defined the “standard Glauber participant eccentricity” in Eq. (13). An equally good definition is provided by collision scaling. For instance, one measure used in heavy ion collisions is the number of binary nucleon-nucleon collisions per transverse area

$$\frac{d^2 N_{\text{coll}}}{dzdy} = \sigma_{\text{NN}} T_A(\mathbf{x} + \mathbf{b}/2) T_A(\mathbf{x} - \mathbf{b}/2), \quad (17)$$

Then the eccentricity is defined with this N_{coll} weight in analogy with Eq. (13). Fig. 7 shows the “standard Glauber N_{coll} eccentricity”. Another more sophisticated

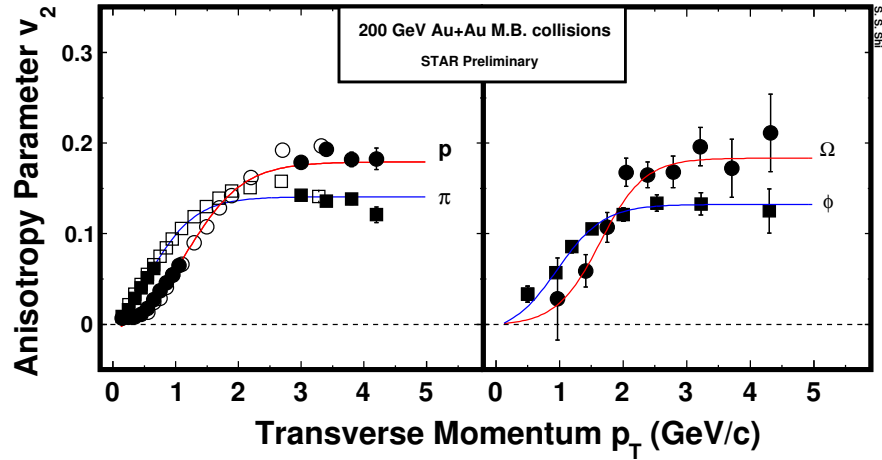


Fig. 6. A comparison of the elliptic flow of pions and protons to the elliptic flow of the multi-strange ϕ and Ω^- hadrons⁴³.

model is provided by the KLN model which is based on the ideas of gluon saturation and the Color Glass Condensate (CGC)^{44,45} as implemented in Refs.^{46,47}. This model is a safe upper bound on what can be expected for the eccentricity from saturation physics and is also shown in Fig. 7. We can not describe the details of this model and its implementation here. However, the physical reason why this model has a sharper eccentricity is the readily understood: the center of one nucleus (nucleus A) passes through the edge of the other nucleus (nucleus B). Since the density of gluons per unit area in the initial wave function is larger in the center of a nucleus relative to the edge, the typical momentum scale of nucleus A ($\sim Q_{s,A}$) is larger nucleus B ($\sim Q_{s,B}$). It is then difficult for the long wavelength (low momentum) gluons in B to liberate the short wavelength gluons in A . The result is that the production of gluons falls off more quickly near the x edge relative to the y edge making the eccentricity larger. Clearly this physics is largely correct although the magnitude of the effect is uncertain. Another CGC estimate of ϵ is based on classical simulations of Yang-Mills fields. The simulations include similar saturation physics but model the production and non-perturbative sectors differently. The eccentricity from these simulations is also shown in Fig. 7 and is similar to the N_{coll} eccentricity⁴⁸. Thus the predictions of the KLN model seem to be a safe upper bound for the eccentricity in heavy ion collisions. Note that an important phenomenological consequence of the the KLN model is that the eccentricity grows with beam energy and is expected to increase about 20% from the RHIC to the

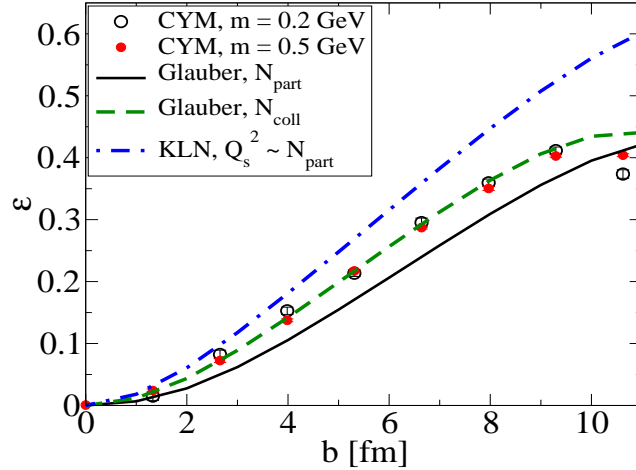


Fig. 7. Figure from Ref.⁴⁸ showing various estimates for the initial eccentricity in heavy ion collisions. The physics of the KLN eccentricity is described in the text. In the KLN model the eccentricity is expected to increase by about 20% when going from RHIC to the LHC⁴¹.

LHC⁴¹.

Another important aspect in heavy ion collisions when interpreting the elliptic flow data is fluctuations in the initial eccentricity. These fluctuations are not accounted for in Fig. 7. The history is complicated and is reviewed in Refs.^{49,37}. There are fluctuations in the initial eccentricity of the participants especially in peripheral AuAu and CuCu collisions. Thus rather than using the continuum approximation given in Eq. (13) it is better to implement a Monte-Carlo Glauber calculation and estimate the eccentricity using the “participant plane eccentricity”. Fig. 8 illustrates the issue: In a given event the ellipse is tilted and the eccentricity depends on the distribution of participants. This event by event eccentricity is denoted ϵ_{PP} in the literature. Clearly the experimental goal is to extract the *response* coefficient C relating the elliptic flow to the eccentricity on an event by event basis

$$v_2 = C\epsilon_{PP}. \quad (18)$$

If the flow methods measured $\langle v_2 \rangle$, then we could simply divide the measured flow to determine the response coefficient, $C = \langle v_2 \rangle / \langle \epsilon_{PP} \rangle$. The PHOBOS collaboration deciphered the confusing CuCu data by recognizing the need for ϵ_{PP} and following this procedure⁵¹. However, it was generally realized (see in particular. Ref.⁵²) that the elliptic flow methods do not measure precisely $\langle v_2 \rangle$. Some methods (such as two particle correlations $v_2\{2\}$) are sensitive to $\sqrt{\langle v_2^2 \rangle}$, while other methods (such as the event plane method $v_2\{EP\}$) measure something closer to $\langle v_2 \rangle$. What precisely the event plane method measures depends on the reaction

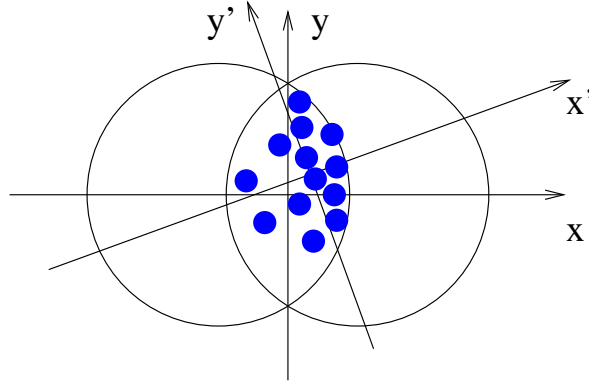


Fig. 8. A figure from Ref.⁵⁰ illustrating the participant plane eccentricity ϵ_{PP} in a single event.

plane resolution in a known way⁴⁹. So just dividing the measured flow by the average participant eccentricity is not entirely correct. The appropriate quantity to divide by depends on the method^{52,50,53}. In a Gaussian approximation for the eccentricity fluctuations this can be worked out analytically. For instance, the two particle correlation elliptic flow $v_2\{2\}$ (which measures $\sqrt{\langle v_2^2 \rangle}$), should be divided by $\sqrt{\langle \epsilon_{PP}^2 \rangle}$. An important corollary of this analysis is that $v_2\{4\}$ (v_2 measured from four particle correlations) can be divided by ϵ_s of Eq. (13) to yield a good estimate of the coefficient C . This is the policy adopted in Fig. 5. Unfortunately, in the most peripheral AuAu bins and in CuCu the Gaussian approximation is poor due to strong correlations amongst the participants⁵⁴. These correlations arise because participants come in pairs and every participant is associated with another participant in the other nucleus. Presumably the last centrality bin in Fig. 5 could be moved up or down somewhat due to non-Gaussian corrections of this sort. With a complete understanding of what each method measures, Ref.⁴⁹ was able to make a simple model for the fluctuations and non-flow and show that $\langle v_2 \rangle$ measured by the different methods are compatible to an extremely good precision. This work should be extended to the CuCu system where non-Gaussian fluctuations are stronger and ultimately corroborate the PHOBOS analysis^{51,54}. This is a worthwhile goal because it will clarify the transition into the hydrodynamic regime⁸.

2.4. Summary

In this section we have gone into considerable experimental detail – perhaps more than necessary to explain the basic ideas. The reason for this lengthy summary is because the trends seen in Fig. 5 were not always so transparent. The relatively coherent hydrodynamic and kinetic interpretation of the observed elliptic flow (which was previewed in Section 2.2 and which is discussed more completely below) is the result of careful experimental analysis.

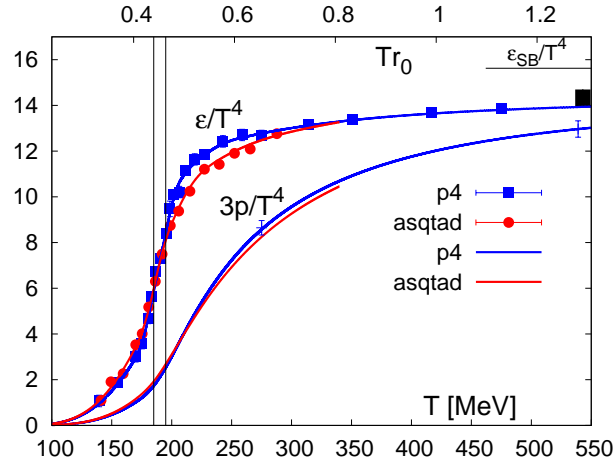


Fig. 9. Figure from Ref.⁵⁵ illustrating the energy density and pressure by T^4 of QCD computed with $N_\tau = 8$ lattice data. (In this figure ϵ is energy density $e(T)$ and the pressure p is denoted with \mathcal{P} throughout this review.) $\epsilon_{SB}/T^4 \equiv e_{SB}/T^4$ is the energy density of a free three flavor massless QGP (see text).

3. The Shear Viscosity in QCD

In this section we will discuss thermal QCD in equilibrium with the primary goal of collecting various theoretical estimates for the shear viscosity in QCD.

The prominent feature of QCD at finite temperature is the presence of an approximate phase transition from hadrons to quarks and gluons. The Equation of State (EoS) from lattice QCD calculations is shown in Fig. 9, and the energy density $e(T)$ shows a rapid change for the temperature range, $T \simeq 170 - 220$ MeV. As estimated in Section 4, the transition region is directly probed during high energy heavy ion collisions.

Well below the phase transition, the gas of hadrons is very dilute and the thermodynamics is dominated by the measured particle spectrum. For instance the number of pions in this low temperatures regime is

$$n_\pi = d_\pi \int \frac{d^3\mathbf{p}}{(2\pi)^3} \frac{1}{e^{E_{\mathbf{p}}/T} - 1}, \quad (19)$$

where $E_{\mathbf{p}} = \sqrt{p^2 + m_\pi^2}$ and $d_\pi = 3$ counts the three fold isospin degeneracy, π^+, π^-, π^0 , in the spectrum. If all known particles are included up to a mass $m_{\text{res}} < 2.5$ GeV, the resulting Hadron Resonance Gas (HRG) equation of state does a reasonable job of reproducing the thermodynamics up to about $T \simeq 180$ MeV. However, the validity of this quasi-particle description is unclear above a temperature of⁵⁶, $T \simeq 140$ MeV. As the temperature increases, the hadron wave functions overlap until the medium reorganizes into quark and gluon degrees of freedom. Well above the transition the QCD medium evolves to a phase of massless quarks and

gluons. The energy density is approximately described by the Stefan-Boltzmann equation of state

$$e_{\text{glue}} = d_{\text{glue}} \int \frac{d^3\mathbf{p}}{(2\pi)^3} \frac{E_{\mathbf{p}}}{e^{E_{\mathbf{p}}/T} - 1}, \quad e_{\text{quark}} = d_{\text{quark}} \int \frac{d^3\mathbf{p}}{(2\pi)^3} \frac{E_{\mathbf{p}}}{e^{E_{\mathbf{p}}/T} + 1}, \quad (20)$$

where $d_{\text{glue}} = 2 \times 8$ counts spin and color, and $d_{\text{quark}} = 2 \times 2 \times 3 \times 3$ counts spin, anti-quarks, flavor, and color. Performing these integrals we find, $e_{SB} = e_{\text{glue}} + e_{\text{quark}} \simeq 15.6 T^4$ as illustrated by the line in the top-right corner of the figure.

We have described the particle content well above and well below the transition. Near the approximate phase transition the validity of such a simple quasi-particle description is not clear. The transition is a rapid cross-over where hadron degrees of freedom evolve into quark and gluon degrees of freedom rather than a true phase transition. All correlators change smoothly, but rapidly, in a temperature range of $T \simeq 170 - 210$ MeV. From a phenomenological perspective the smoothness of the transition suggests that the change from quarks to hadrons should be thought of as a soft process rather than an abrupt change.

Lattice QCD simulations have determined the equation of state rather well. However, in addition to the equation of state, we need to estimate the transport coefficients to assess whether the heavy ion reactions produce enough material, over a large enough space-time volume to be described in thermodynamic terms. The shear and bulk viscosities govern the transport of energy and momentum and are clearly the most important.

Later in Section 4 and Section 5 we will describe the role of shear viscosity in the reaction dynamics. In this section we summarize the shear viscosities found in various theoretical computations which will place these dynamical conclusions in context. A good way to implement this theoretical summary is to form shear viscosity to entropy ratio¹⁵, η/s . To motivate this ratio we remark that it seems difficult to transport energy faster than a quantum time scale set by the inverse temperature^a,

$$\tau_{\text{quant}} \sim \frac{\hbar}{k_B T}.$$

A sound wave propagating with speed c_s will diffuse (or spread out) due to the shear viscosity. Linearized hydrodynamics shows that this process is controlled by the momentum diffusion coefficient, $D_\eta \equiv \eta/(e + \mathcal{P})$, where $e + \mathcal{P}$ is the enthalpy (see for example Ref.⁵⁷). Noting that the diffusion coefficient has units of (distance)²/time, a kinetic theory estimate for the diffusion process yields

$$D_\eta \equiv \frac{\eta}{e + \mathcal{P}} \sim v_{\text{th}}^2 \tau_R, \quad (21)$$

where τ_R is the particle relaxation time and $v_{\text{th}}^2 \sim c_s^2$ is the particle velocity. Dividing by v_{th}^2 and using the thermodynamic estimates

$$sT \sim e v_{\text{th}}^2 \sim \mathcal{P} \sim n k_B T, \quad (22)$$

^aIn this paragraph we will restore \hbar and the Boltzmann constant, k_B .

we see that

$$\frac{\eta}{s} \sim \tau_R T \sim \frac{\hbar}{k_B} \frac{\tau_R}{\tau_{\text{quant}}}. \quad (23)$$

Therefore, η/s is the ratio between the medium relaxation time and the quantum time scale τ_{quant} in units of \hbar/k_B , *i.e.* a measure of the transport time in “natural units”.

In the dilute regime the ratio between the medium relaxation time and the quantum time scale is long and kinetic theory can be used to calculate the shear viscosity to entropy ratio. First we consider a simple classical massless gas with particle density n and a constant hard sphere cross section σ_o . The equation of state of this gas is $e = 3\mathcal{P} = 3nT$ and the shear viscosity is computed using kinetic theory⁵⁸

$$\eta \simeq 1.2 \frac{T}{\sigma_o}, \quad (24)$$

The entropy is $s = (e + \mathcal{P})/T$ and the resulting shear to entropy ratio is

$$\frac{\eta}{s} \simeq 0.3 \frac{T}{n\sigma_o}. \quad (25)$$

In what follows, this calculation will provide a qualitative understanding of more sophisticated kinetic calculations.

In the dilute hadronic regime, η/s was calculated in Ref.⁵⁹ using measured elastic cross sections for a gas of pions and kaons. In the $\pi\pi$ phase shifts there is a prominent ρ resonance, while in the πK channel there is a prominent K^* resonance. Thus the equation of state of this gas is well modeled by an ideal gas of π, K, ρ and K^* ^{60,61}. The viscosity of this mixture was computed in Ref.⁵⁹ and the current author digitized this viscosity, computed the entropy, and determined the η/s ratio. This is shown in Fig. 10. Slightly larger values were obtained in Ref.⁵⁶ which also estimated the range of validity for hadronic kinetic theory, $T \lesssim 140$ MeV. Finally a more involved Kubo analysis of the UrQMD hadronic transport model⁶² (which includes many resonances) is also displayed in Fig. 10.

At asymptotically high temperatures the coupling constant α_s is weak and the shear viscosity can be computed using perturbation theory. Initially, only $2 \rightarrow 2$ elastic scattering was considered, and the shear viscosity was computed in a leading log plasma with self consistent screening⁶⁴. Later it was recognized^{65,66} that collinear Bremsstrahlung processes are important for the calculation of shear viscosity and this realization ultimately resulted in a complete leading order calculation⁶³. We can estimate η/s in the perturbative plasma using Eq. (24) with $s \propto T^3$ and $\sigma \propto \alpha_s^2/T^2$,

$$\frac{\eta}{s} \sim \frac{1}{\alpha_s^2}. \quad (26)$$

The final result from a complete calculation has the form

$$\frac{\eta}{s} = \frac{1}{\alpha_s^2} F(m_D/T), \quad (27)$$

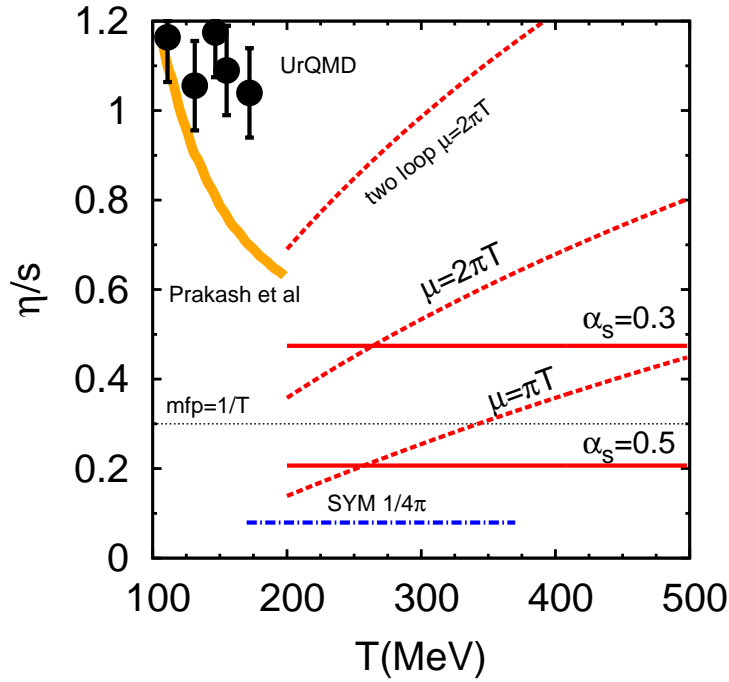


Fig. 10. (Color Online) A compilation of values of η/s . The results from Prakash *et al* are from Ref.⁵⁹ and describe a meson gas of pions and kaons (and indirectly K^* and ρ) computed with measured cross sections. The black points are based on a Kubo analysis of the UrQMD code which includes many higher resonances⁶². The red lines are different implementations of the AMY (Arnold, Moore, Yaffe) calculation of shear viscosity⁶³. In each curve the Debye scale is fixed $m_D = 2T$. In the dashed red curves the (one loop three flavor) running coupling is taken at the scale μ . In the solid red curves α_s is kept fixed. The two loop running coupling is shown with $\mu = 2\pi T$ for comparison and the two loop $\mu = \pi T$ (not shown) is similar to the one loop $\mu = 2\pi T$ result. In the AMY curves, changing the Debye mass by $\pm 0.5T$ changes η/s by $\sim \pm 30\%$. Finally the thin dashed line indicates a simple model discussed in the text with $\ell_{\text{mfp}} = 1/T$.

where $F(m_D/T)$ is a function of the Debye mass which was computed for m_D/T small and then extrapolated to more realistic values⁶³. There are many scales in the problem and it is difficult to know what precisely to take for the Debye mass and the coupling constant. At lowest order in the coupling, the Debye mass is⁶⁷

$$m_D^2 = \left(\frac{N_c}{3} + \frac{N_f}{6} \right) g^2 T^2, \quad (28)$$

but this is too large to be considered reliable. For definiteness we have evaluated the leading coupling constant in Eq. (27) at a scale of πT and set the Debye mass to $m_D = 2T$. The resulting value of η/s is shown in Fig. 10. Various other alternatives are explored in the figure and underscore the ambiguity in these numbers.

Clearly all of the calculations presented have a great deal of uncertainty around

the phase transition region. On the hadronic side there are a large number of inelastic reactions which become important. On the quark gluon plasma side, the strong dependence on the Debye scale and the coupling constant is disconcerting. It is very useful to have a strongly coupled theory where the shear viscosity to entropy ratio can be computed exactly. In strongly coupled $\mathcal{N} = 4$ SYM theory with a large number of colors, η/s can be computed using gauge gravity duality and yields the result^{14,15}

$$\frac{\eta}{s} = \frac{1}{4\pi}. \quad (29)$$

From the perspective of heavy ion physics this result was important because it showed that there exist field theories where η/s can be this low. Although $\mathcal{N} = 4$ has no particle interpretation, we note that extrapolating Eq. (24) by setting $\ell_{\text{mfp}} = 1/n\sigma_o = 1/\pi T$ yields a value for η/s which is approximately equal to the SYM result. In Fig. 10 we have displayed this numerology with $\ell_{\text{mfp}} = 1/T$ for clarity.

There are many aspects of transport coefficients which have not been reviewed here. For instance, there is an ongoing effort to determine the transport coefficients of QCD from the lattice^{68,69}. While a precise determination of the transport coefficients is very difficult^{70,71,57}, the lattice may be able to determine enough about the spectral densities to distinguish the orthogonal pictures represented by $\mathcal{N} = 4$ SYM theory and kinetic theory⁶⁸. This is clearly an important goal and we refer to Ref.⁷² for theoretical background. Also throughout this review we have emphasized the shear viscosity and neglected the bulk viscosity. This is because on the hadronic side of the phase transition the bulk viscosity is a thousand times smaller than the shear viscosity in the regime where it can be reliably calculated⁵⁹. Similarly on the high temperature QGP side of the phase transition the bulk viscosity is also a thousand times smaller than shear⁷³. However, near a second order phase transition the bulk viscosity can become very large^{74,75,76}. Nevertheless the rapid cross-over seen in Fig. 9 is not particularly close to a second order phase transition and universality arguments can be questioned (see Ref.⁵⁵ for a discussion in the context of the chiral susceptibility.) Given the ambiguity at this moment it seems prudent to leave the bulk viscosity to future review.

4. Hydrodynamic Description of Heavy Ion Collisions

In the previous sections we analyzed the phase diagram of QCD and estimated the transport coefficients in different phases. In this section we will study the hydrodynamic modeling of heavy ion collisions.

In Section 4.2 we will consider ideal hydrodynamics and assume that the mean free paths are small enough to support this interpretation. Subsequently we will study viscous hydrodynamics in Section 4.3. Section 4.4 will analyze the ratio of the viscous terms to the ideal terms and use the estimates of the transport coefficients given above to assess the validity of the hydrodynamic interpretation. Section 4.6

will discuss the recent advances in interpreting the hydrodynamic equations beyond the Navier Stokes limit. This work will lay the foundation for the more detailed hydrodynamic models presented in Section 6.

4.1. *Ideal Hydrodynamics*

The stress tensor of an ideal fluid and its equation of motion are simply

$$T^{\mu\nu} = eu^\mu u^\nu + \mathcal{P}\Delta^{\mu\nu}, \quad \partial_\mu T^{\mu\nu} = 0, \quad (30)$$

where e is the energy density, $\mathcal{P}(e)$ is the pressure, and $u^\mu = (\gamma, \gamma\mathbf{v})$ is the four velocity. Here we will use the metric $(-, +, +, +)$ and define the projection tensor, $\Delta^{\mu\nu} = g^{\mu\nu} + u^\mu u^\nu$, with $u^\mu u_\mu = -1$ and $\Delta^{\mu\nu} u_\mu = 0$. This decomposition of the stress tensor is simply a reflection of the fact that in the local rest frame of a thermalized medium the stress tensor must have the form, $\text{diag}(e, \mathcal{P}, \mathcal{P}, \mathcal{P})$. In developing viscous hydrodynamics we will define two derivatives which are the time derivative D , and the spatial derivatives ∇^μ in the local rest frame

$$D \equiv u^\mu \partial_\mu, \quad \nabla^\mu \equiv \Delta^{\mu\nu} \partial_\nu. \quad (31)$$

Using $\partial_\mu = -u_\mu D + \nabla_\mu$ and $u_\mu D u^\mu = 0$, the ideal equations of motion can be written

$$De = -(e + \mathcal{P})\nabla_\mu u^\mu, \quad (32)$$

$$Du^\mu = -\frac{\nabla^\mu \mathcal{P}}{e + \mathcal{P}}. \quad (33)$$

The first equation says that the change in energy density is due to the $\mathcal{P}dV$ work or equivalently that entropy is conserved. To see this we associate $\nabla_\mu u^\mu$ with the fractional change in volume per unit time in the co-moving frame, $dV/V = dt \times \nabla_\mu u^\mu$, and use the thermodynamic identity, $d(eV) = Td(sV) - \mathcal{P}dV$. The second equation says that the acceleration is due to the gradients of pressure. The enthalpy plays the role of the mass density in a relativistic theory.

4.2. *Ideal Bjorken Evolutions and Three Dimensional Estimates*

In this section we will follow an analysis due to Bjorken⁷⁷ and apply ideal hydrodynamics to heavy ion collisions. Bjorken's analysis was subsequently extended in important ways^{78,13,79}. In a high energy heavy ion collisions the two nuclei pass through each other and the partons are scarcely stopped. This statement underlies much of the interpretation of high energy events and an enormous amount of data is consistent with this assumption. For a time which is short compared to the transverse size of the nucleus, the transverse expansion can be ignored.

Given that the nuclear constituents pass through each other, the longitudinal momentum is much much larger than the transverse momentum. Because of this scale separation there is a strong identification between the space-time coordinates

and the typical z momentum. For example a particle with typical momentum p_z and energy E will be found in a definite region of space time

$$v^z = \frac{p^z}{E} \simeq \frac{z}{t}. \quad (34)$$

This kinematics is best analyzed with proper time and space-time rapidity variables^b, τ and η_s

$$\tau \equiv \sqrt{t^2 - z^2}, \quad \eta_s \equiv \frac{1}{2} \log \left(\frac{t+z}{t-z} \right).$$

At a proper time τ particles with rapidity y are predominantly located at space time rapidity η_s

$$y \equiv \frac{1}{2} \log \frac{p_z + E}{E - p_z} \simeq \frac{1}{2} \log \frac{t+z}{t-z} \equiv \eta_s. \quad (35)$$

Fig. 11 illustrates these coordinates and shows schematically the identification between η_s and y . At an initial proper time τ_o , there is a collection of particles predominantly moving with four velocity u^μ in each space-time rapidity slice

$$\frac{1}{2} \log \left(\frac{u^0 + u^z}{u^0 - u^z} \right) \simeq \eta_s. \quad (36)$$

The beam rapidity at RHIC is $y_{\text{beam}} \simeq 5.3$ and therefore roughly speaking the particles are produced in the space-time rapidity range $-5.3 < \eta_s < 5.3$. It is important to realize that (up to about a unit or so) each space-time rapidity slice is associated with a definite angle in the detector. For ultra-relativistic particles $E \simeq p$ we have

$$\eta_s \simeq y \simeq \frac{1}{2} \log \left(\frac{p + p_z}{p - p_z} \right) = \frac{1}{2} \log \left(\frac{1 + \cos \theta}{1 - \cos \theta} \right) \equiv \eta_{\text{pseudo}}, \quad (37)$$

where a particular θ is shown in Fig. 1. The measured pseudo-rapidity distribution of charged particles is shown in Fig. 12. We can estimate the energy in a unit of pseudo-rapidity by taking $\langle E \rangle \simeq 0.5 \text{ GeV}$ as the energy per particle. Then the energy in a pseudo-rapidity unit is

$$\frac{dE}{d\eta_{\text{pseudo}}} \simeq \langle E \rangle \frac{dN_{\text{ch}}}{d\eta_{\text{pseudo}}} \times 1.5 \simeq 3.0 \text{ GeV} \times (N_p/2),$$

where $(N_p/2) \simeq 170$ is the number of participant pairs in a central event. The factor of 1.5 has been inserted to account for the fact that there are approximately equal numbers of π^+ , π^- and π^0 (the most abundant particle) but only π^+ and π^- are counted in $dN_{\text{ch}}/d\eta_{\text{pseudo}}$. This estimate agrees reasonably with the measured $dE_T/d\eta_{\text{pseudo}} \simeq 3.2 \text{ GeV} \times N_p/2$ from Ref.⁸⁰.

^b Here η_s denotes the space time rapidity, η_{pseudo} denotes the pseudo-rapidity (see below), η denotes the shear viscosity. In raised space time indices in τ, η_s coordinates we will omit the ‘‘s’’ when confusion can not arise, e.g. $\pi^{\eta\eta} = \pi^{\eta_s\eta_s}$.

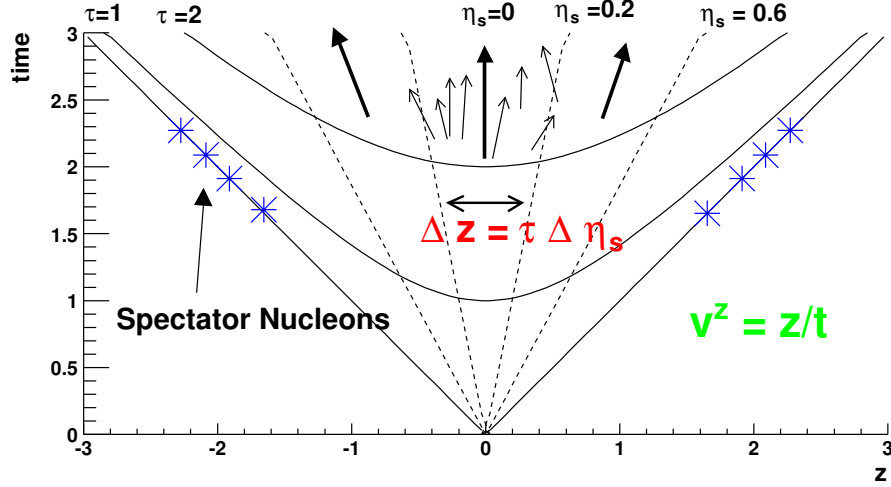


Fig. 11. A figure motivating for the Bjorken model. The space between the dashed lines of constant η_s are referred to as a space-time rapidity slice in the text. Lines of constant proper time τ are given by the solid hyperbolas. The collection of particles in the $\eta_s = 0$ rapidity slice is indicated by the small arrows for the central ($\eta_s = 0$) rapidity slice only. The solid arrows indicates the average four velocity u^μ in each slice. The spectators are those nucleons which do not participate in the collision and lie along the light cone.

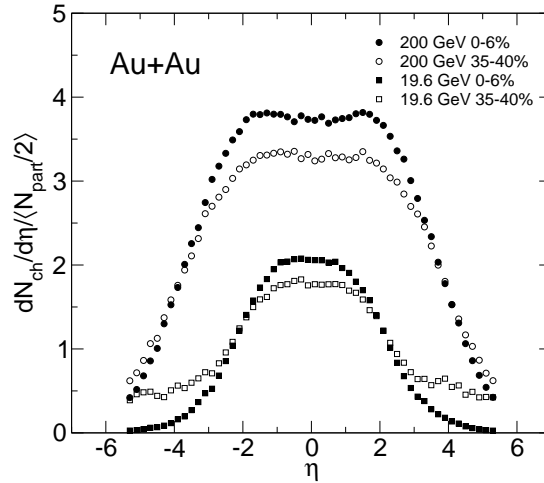


Fig. 12. The measured charged particle pseudo-rapidity distribution $dN_{\text{ch}}/d\eta_{\text{pseudo}}$ for different beam energies divided by the number of participant pairs, $N_p/2$. $N_p/2 \simeq 170$ for a central (0-6%) AuAu collision. This review focuses on $\sqrt{s} = 200$ GeV/nucleon.

Bjorken used these kinematic ideas to estimate the initial energy density in the $\eta_s = 0$ rapidity slice at an initial time, $\tau_0 \simeq 1$ fm. The estimate is based on the fairly

well supported assumption that the energy which finally flows into the detector $dE_T/d\eta_{\text{pseudo}}$ largely reflects the initial energy in a given space-time rapidity slice

$$\epsilon_{Bj} \simeq \frac{1}{A} \frac{\Delta E}{\Delta z} \simeq \frac{1}{A\tau_o} \frac{\Delta E}{\Delta\eta_s} \simeq \frac{1}{A\tau_o} \frac{dE_T}{d\eta_{\text{pseudo}}}, \quad (38)$$

$$\simeq 5.5 \frac{\text{GeV}}{\text{fm}^3}. \quad (39)$$

In the last line we have estimated the area of a gold nucleus as $A \simeq 100 \text{ fm}^2$, taken $\tau_o \simeq 1 \text{ fm}$, and used the measured $dE_T/d\eta_{\text{pseudo}}$. This estimate is generally considered a lower limit since during the expansion there is $\mathcal{P}dV$ work as the particles in one rapidity slice push against the particles in another rapidity slice^{13,78,79} (See Fig. 11). Using the equation of state in Fig. 9 we estimate an initial temperature, $T(\tau_o) \simeq 250 \text{ MeV}$. As mentioned above this estimate is somewhat low for hydrodynamic calculations and a more typical temperature is $T \simeq 310 \text{ MeV}$, which has roughly twice the Bjorken density²⁴.

As seen in Fig. 12, the distribution of the energy density $e(\tau_o, \eta_s)$ in space-time rapidity is not uniform. In the Color Glass Condensate (CGC) picture for instance, the final distribution of multiplicity is related to the x distribution of partons inside the nucleus⁴⁴. Bjorken made the additional simplifying assumption that the energy density is uniform in space-time rapidity, *i.e.* $e(\tau_o, \eta_s) \simeq e(\tau_o)$. With this simplification, the identification between the fluid and space time rapidities remains fixed as the fluid flows into the forward light cone.

We have discussed the motivation for the Bjorken model. Formally the model consists of the following ansatz for the hydrodynamic variables

$$e(t, \mathbf{x}) = e(\tau), \quad u^\mu(t, \mathbf{x}) = (u^0, u^x, u^y, u^z) = (\cosh(\eta_s), 0, 0, \sinh(\eta_s)). \quad (40)$$

The model is invariant under boosts in the z direction. Thus given a physical quantity at mid-rapidity ($\eta_s = 0$), one can determine this quantity at all other rapidities by a longitudinal boost. We will use curvilinear coordinates where⁸¹

$$x^\mu = (\tau, \mathbf{x}_\perp, \eta_s), \quad g_{\mu\nu} = \text{diag}(-1, 1, 1, \tau^2), \quad (u^\tau, u^x, u^y, u^\eta) = (1, 0, 0, 0). \quad (41)$$

In this coordinate system boost invariance implies that everything is independent of η_s . To interpret a tensorial component in these coordinates, we multiply by $\sqrt{g_{\eta\eta}} = \tau$ for every raised η_s index, and subsequently associate the product with the corresponding cartesian component at mid-rapidity. For example, $\tau^2 T^{\eta\eta} = T^{zz}|_{\eta_s=0} = \mathcal{P}$. Similarly, $\tau u^\eta = u^z|_{\eta_s=0} = 0$ for boost invariant flow.

Substituting the boost invariant ansatz (Eq. (40)) into the conservation laws yields the following equation for the energy density^c

$$\frac{de}{d\tau} = -\frac{e + \mathcal{P}}{\tau}. \quad (42)$$

^cA quick way to derive this is to work in a neighborhood of $z = \eta_s = 0$ where $u^z \simeq z/t$. Substituting this approximate form into $\partial_\mu T^{\mu\nu} = 0$ in cartesian coordinates, quickly yields Eq. (42) with the replacement $t \rightarrow \tau$.

22 *Derek A. Teaney*

Multiplying this equation by the volume of a space time rapidity slice $V = \tau \Delta \eta_s A$ (see Fig. 11) we find

$$d(e \tau \Delta \eta_s A) = -\mathcal{P} d(\tau \Delta \eta_s A), \quad (43)$$

and we can interpret this result¹³ as saying that the energy energy per unit space-time rapidity ($e \tau \Delta \eta_s A$) decreases due to the $\mathcal{P}dV$ work. It is for this reason that the Bjorken estimate e_{Bj} (which assumes that the r.h.s. of Eq. (43) equals zero) should be considered a lower bound. In general, assuming Bjorken scaling (Eq. (40)) and the conservation laws, but not assuming local thermal equilibrium, one finds

$$\frac{de}{d\tau} = -\frac{e + T^{zz}}{\tau}, \quad (44)$$

where $T^{zz} \equiv \tau^2 T^{\eta\eta}$ is the effective longitudinal pressure. Viscous corrections will modify T^{zz} from its equilibrium value of \mathcal{P} .

Returning to the equilibrium case, Eq. (42) can be solved for a massless ideal gas equation of state ($e = 3\mathcal{P} \propto T^4$) and the time dependence of the temperature is

$$T(\tau) = T_o \left(\frac{\tau_o}{\tau} \right)^{1/3}, \quad (45)$$

where T_o is the initial temperature. The temperature decreases rather slowly as a function of proper time during the initial one dimensional expansion. This will turn out to be important when discussing equilibration. For a massless ideal gas, the entropy is $s = (e + \mathcal{P})/T \propto T^3$ and decreases as

$$s(\tau) = s_o \frac{\tau_o}{\tau}. \quad (46)$$

Now we discuss what happens when the initial energy density distribution is not uniform in rapidity. Due to pressure gradients in the longitudinal direction, there is some longitudinal acceleration. This changes the strict identification between the space time rapidity and the fluid rapidity given in Eq. (36). It also changes the temperature dependence given above. One way to quantify this effect is to look at the results of 3D ideal hydrodynamic calculations and study the differences between the initial energy distribution in space-time rapidity $\int d^2 \mathbf{x}_\perp e(\tau_o, \mathbf{x}_\perp, \eta_s)$ and the final energy distribution, $\int d^2 \mathbf{x}_\perp e(\tau_f, \mathbf{x}_\perp, \eta_s)$. Generally, the final distribution in space-time rapidity is similar to the initial distribution in space-time rapidity^{18,82}. Therefore, the effect of longitudinal acceleration is unimportant until late times.

The nuclei have a finite transverse size, $R_{Au} \sim 6$ fm. After a time of order

$$\tau \sim \frac{R_{Au}}{c},$$

the expansion becomes three dimensional. To estimate how the temperature evolves during the course of the resulting 3D expansion, consider a sphere of radius R which expands in all three directions. The radius and volume increase as

$$R \propto \tau, \quad V \propto \tau^3.$$

Since for an ideal expansion the total entropy in the sphere is constant, the entropy density decreases as $1/\tau^3$ and the temperature decreases as

$$s \propto \frac{1}{\tau^3}, \quad T \propto \frac{1}{\tau}. \quad (47)$$

Here we have estimated how the entropy decreases during a one and three dimensional expansion of an ideal massless gas. Now if during the course of the collision there are non-equilibrium processes which generate entropy that ultimately equilibrates, the temperature of this final equilibrated gas will be larger than if the expansion was isentropic. Effectively the temperature will decrease more slowly. To estimate this effect in a one dimensional expansion, we imagine a free streaming gas where the longitudinal pressure is zero. Then from Eq. (42) we have

$$\frac{de}{d\tau} \sim \frac{e}{\tau}. \quad (48)$$

In the sense discussed above, this equation may be integrated to estimate that the temperature and entropy decrease as

$$T \propto \frac{1}{\tau^{1/4}}, \quad s \propto \frac{1}{\tau^{3/4}}. \quad (49)$$

Similarly in a three dimensional expansion we can estimate how entropy production will change the powers given in Eq. (47). Again consider a sphere of radius R which expands in all three directions, such that $R \propto \tau$ and $V \propto \tau^3$. For a free expansion without pressure the total energy in the sphere is constant, and the energy density decreases as $1/\tau^3$. Similarly, we estimate that the temperature and entropy density decrease as

$$T \propto \frac{1}{\tau^{3/4}}, \quad s \propto \frac{1}{\tau^{9/4}}. \quad (50)$$

In summary we have estimated how the temperature and entropy density depend on the proper time τ during the course of an ideal and non-ideal 1D and 3D expansion. This information is recorded in Table 1. These estimates are also nicely realized in actual hydrodynamic simulations. Fig. 13 shows the dependence of entropy density as a function of proper time τ . The figure indicates that the entropy decreases as $1/\tau$ during an initial one dimensional expansion and subsequently decreases as $1/\tau^3$ when the expansion becomes three dimensional at a time of order ~ 5 fm. These basic rules will be useful when estimating the relative size of viscous terms in what follows.

4.3. Viscous Bjorken Evolution and Three Dimensional Estimates

This section will analyze viscosity in the context of the Bjorken model with the primary goal of assessing the validity of hydrodynamics in heavy ion collisions. In viscous hydrodynamics the stress tensor is expanded in all possible gradients. Using lower order equations of motion any time derivatives of conserved quantities can

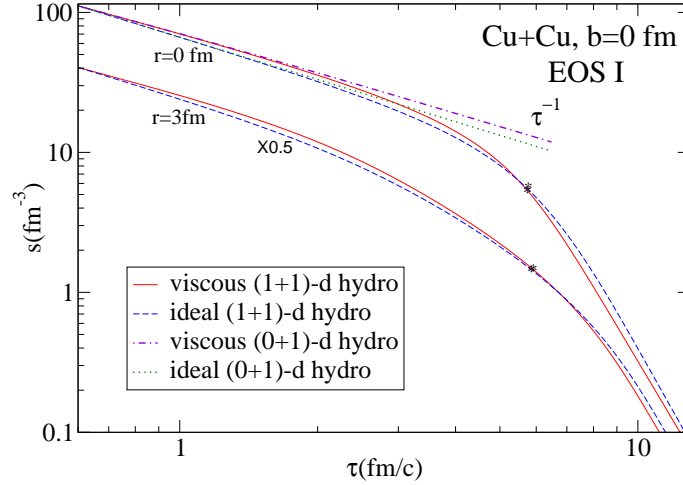


Fig. 13. Figure from Ref.⁹ showing the entropy density (s) in CuCu simulations as a function of proper time τ using ideal and viscous hydrodynamics. The top set of lines shows the entropy in the center of the nucleus-nucleus collision, ($r = 0$ fm), and the bottom set of lines shows the analogous curves closer to the edge ($r = 3$ fm). During an initial one dimensional expansion the entropy density decreases as $s \propto 1/\tau$. Subsequently the entropy decreases as $s \propto 1/\tau^3$ when the expansion becomes three dimensional at a time, $\tau \sim 5$ fm. The lines labeled by (0 + 1) ideal and (0 + 1) viscous are representative of the ideal and viscous Bjorken results Eq. (42) and Eq. (55) respectively.

Quantity	1D Expansion	3D Expansion
T	$(\frac{1}{\tau})^{1/3 \div 1/4}$	$(\frac{1}{\tau})^{1 \div 3/4}$
$s \propto T^3$	$(\frac{1}{\tau})^{1 \div 3/4}$	$(\frac{1}{\tau})^{3 \div 9/4}$

Table 1. Dependence of temperature and entropy as a function of time in a 1D and 3D expansion. The indicated range, for instance $1/3 \div 1/4$, is an estimate of how extreme non-equilibrium effects could modify the ideal power from $1/3$ to $1/4$.

be rewritten as spatial derivatives. First the stress tensor is decomposed into ideal and viscous pieces

$$T^{\mu\nu} = T_{\text{ideal}}^{\mu\nu} + \pi^{\mu\nu} + \Pi \Delta^{\mu\nu}, \quad (51)$$

where $T_{\text{id}}^{\mu\nu}$ is the ideal stress tensor (Eq. (30)) and Π is the bulk stress. $\pi^{\mu\nu}$ is the symmetric traceless shear tensor and satisfies the orthogonality constraint, $\pi^{\mu\nu} u_\nu = 0$. The equations of motion are the conservation laws $\partial_\mu T^{\mu\nu} = 0$ together with a constituent relation. The constituent relation expands $\pi^{\mu\nu}$ and Π in terms gradients of the conserved charges T^{00} and T^{0i} or their thermodynamic conjugates, temperature T and four velocity u^μ . To first order in this expansion,

the equations of motion are

$$\partial_\mu T^{\mu\nu} = 0, \quad \pi^{\mu\nu} = -\eta\sigma^{\mu\nu}, \quad \Pi = -\zeta\nabla_\mu u^\mu, \quad (52)$$

where η and ζ are the shear and bulk viscosities respectively, and we have defined the symmetric traceless combination

$$\sigma^{\mu\nu} = \nabla^\mu u^\nu + \nabla^\nu u^\mu - \frac{2}{3}\Delta^{\mu\nu}\nabla_\lambda u^\lambda. \quad (53)$$

For later use we also define the bracket $\langle \dots \rangle$ operation

$$\langle A^{\mu\nu} \rangle \equiv \frac{1}{2}\Delta^{\mu\alpha}\Delta^{\nu\beta}(A_{\alpha\beta} + A_{\beta\alpha}) - \frac{1}{3}\Delta^{\mu\nu}\Delta^{\alpha\beta}A_{\alpha\beta}, \quad (54)$$

which takes a tensor and renders it symmetric, traceless and orthogonal to u^μ . Note that $\sigma^{\mu\nu} = 2\langle\partial^\mu u^\nu\rangle$.

We now extend the Bjorken model to the viscous case following Ref.¹³. The bulk viscosity is neglected in the following analysis and we refer to Section 3 for a more complete discussion. Substituting the Bjorken ansatz (Eq. (40)) into the conservation laws and the associated constituent relation (Eq. (52)) yields the time evolution of the energy density

$$\frac{de}{d\tau} = -\frac{e + \mathcal{P} - \frac{4}{3}\eta/\tau}{\tau}. \quad (55)$$

The system is expanding in the z direction and consequently the pressure in the z direction is reduced from its ideal value. Formally this arises due to the gradient $\partial_z u^z = 1/\tau$ and the constituent relation Eq. (52)

$$T^{zz} = \mathcal{P} - \frac{4}{3}\frac{\eta}{\tau}. \quad (56)$$

Thus during a viscous Bjorken expansion the system will do less longitudinal work than in the ideal case.

4.4. The Applicability of Hydrodynamics and η/s

Comparing the viscous equation of motion Eq. (55) to the ideal equation of motion Eq. (42), we see that the hydrodynamic expansion is controlled by

$$\frac{\eta}{e + \mathcal{P}} \frac{1}{\tau} \ll 1. \quad (57)$$

This is a very general result and is a function of time and temperature. Using the thermodynamic relation $e + \mathcal{P} = sT$, we divide this condition into a constraint on a medium parameter η/s and a constraint on an experimental parameter $1/\tau T$

$$\underbrace{\frac{\eta}{s}}_{\text{medium parameter}} \times \underbrace{\frac{1}{\tau T}}_{\text{experimental parameter}} \ll 1. \quad (58)$$

If the experimental conditions are favorable enough, it is appropriate to apply hydrodynamics regardless of the value of η/s . This is the case for sound waves in air

where although η/s is significantly larger than the quantum bound, hydrodynamics remains a good effective theory. However, for the application to heavy ion collisions, the experimental conditions are so unfavorable that only if η/s is close to the quantum bound will hydrodynamics be an appropriate description.

For instance, we estimated the experimental condition in Section 4.1

$$\frac{1}{\tau_o T_o} = 0.66 \left(\frac{1 \text{ fm}}{\tau_o} \right) \left(\frac{300 \text{ MeV}}{T_o} \right). \quad (59)$$

Here we have evaluated this experimental parameter at a specific initial time τ_o and will return to the time evolution of these estimates in the next section. In Section 3 we estimated the medium parameter η/s and can now place these results in context

$$0.2 \left(\frac{\eta/s}{0.3} \right) \left(\frac{1 \text{ fm}}{\tau_o} \right) \left(\frac{300 \text{ MeV}}{T_o} \right) \ll 1. \quad (60)$$

From this condition we see that hydrodynamics will begin to be a good approximation for $\eta/s \lesssim 0.3$ or so. This estimate is borne out by the more detailed calculations presented in Section 6. Reexamining Fig. 10, we see that the value of $\eta/s \simeq 0.3$ is at the low end of the perturbative QGP estimates given in the figure and it is difficult to reconcile the observation of strong collective flow with a quasi-particle picture of quarks and gluons. Thus the estimates of η/s coming from the RHIC experiments, which are based on the hydrodynamic interpretation of the observed flow, should be accepted only with considerable care.

4.5. *Time Evolution*

In the previous section we have estimated the applicability of hydrodynamics at a time $\tau_o \approx 1 \text{ fm}$. In this section we will estimate how the size of the viscous terms depends on time. For this purpose we will keep in mind a kinetic theory estimate for the shear viscosity

$$\eta \sim \frac{T}{\sigma}, \quad (61)$$

and estimate how the gradient expansion parameter in Eq. (55) depends on time. We will contrast a conformal gas with $\sigma \propto 1/T^2$ (*e.g.* perturbation theory or $\mathcal{N} = 4$ SYM) to a gas with fixed cross section, $\sigma = \sigma_o$. There are clearly important scales in the quark gluon plasma as the medium approaches the transition point. For instance spectral densities of current-current correlators near the transition point show a very discernible correlation where the ρ meson will form in the hadron phase^{83,84,69}. Thus the intent of studying this extreme limit with a constant cross section is to show some of the possible effects of these scales. Further the constant cross section kinetic theory has been used to analyze the centrality dependence of elliptic flow⁸.

First consider a theory where the temperature T is the only scale and also consider a 1D Bjorken expansion. The shear viscosity is proportional to T^3 and the

enthalpy scales as T^4 , so the hydrodynamic expansion parameter scales as

$$\frac{\eta}{(e + \mathcal{P})\tau} \sim \frac{1}{\tau T} \sim \frac{1}{\tau^{2/3}}. \quad (62)$$

In the last step we have used the fact that for a scale invariant gas undergoing an ideal Bjorken expansion the temperature decreases as $1/\tau^{1/3}$. In general if we have some non-equilibrium processes which produce entropy during the course of the expansion, the temperature will decrease more slowly than estimated in the ideal gas case – see Table 1. The result is that we do not expect the temperature to decrease more slowly than $1/\tau^{1/4}$, and we can estimate that the hydrodynamic expansion parameter evolves as

$$\frac{\eta}{(e + \mathcal{P})\tau} \propto \frac{1}{\tau T} \propto \frac{1}{\tau^{2/3 \div 3/4}}. \quad (63)$$

Thus during a 1D expansion of a conformal gas the system will move closer to equilibrium.

Compare this scale invariant theory to a gas with a very definite cross section σ_o . For a constant σ_o the hydrodynamic expansion parameter evolves as

$$\frac{\eta}{(e + \mathcal{P})\tau} \propto \frac{1}{s\sigma\tau} \propto \left(\frac{1}{\tau}\right)^{0 \div 1/4}. \quad (64)$$

Thus, with a constant cross section, the gas will move neither away nor toward equilibrium as a function of time. Non-equilibrium physics will make the matter evolve slowly toward equilibrium.

Now we will compute the analogous effects for a three dimensional expansion. In the conformal case $\eta \propto T^3$ and $T \propto \frac{1}{\tau}$, so that the final result is

$$\frac{\eta}{(e + \mathcal{P})\tau} \propto \frac{1}{\tau T} \propto \left(\frac{1}{\tau}\right)^{0 \div 1/4}. \quad (65)$$

Thus a conformal gas expanding isentropically in three dimensions also moves neither away nor towards equilibrium, though entropy production will cause it to slowly equilibrate. Similarly for gas with a constant cross section the hydrodynamic parameter evolves as

$$\frac{\eta}{(e + \mathcal{P})\tau} \propto \frac{1}{s\sigma\tau} \propto \tau^{2 \div 5/4}. \quad (66)$$

In estimating this last line we have used Table 1. Thus we see that a gas with fixed cross-sections which expands in three dimensions very rapidly breaks up.

The preceding results are summarized in Table 2. Essentially the heavy ion collision proceeds along the following line of reasoning. First, there is a one dimensional expansion where the temperature is the dominant scale in the problem. The parameter which controls the applicability of hydrodynamics $\eta/[(e + \mathcal{P})\tau]$ decreases as a function of time; hydrodynamics gets better and better, evolving according to the upper left corner of Table 2. As the system expands and cools toward the transition region additional scales enter the problem. Typically at this point $\tau \sim 4$ fm/c the

Model	1D Expansion	3D Expansion
$\eta \propto T^3$	$\frac{\eta}{(e+\mathcal{P})\tau} \propto \left(\frac{1}{\tau}\right)^{2/3 \div 3/4}$	$\frac{\eta}{(e+\mathcal{P})\tau} \propto \left(\frac{1}{\tau}\right)^{0 \div 1/4}$
$\eta \propto \frac{T}{\sigma_o}$	$\frac{\eta}{(e+\mathcal{P})\tau} \propto \left(\frac{1}{\tau}\right)^{0 \div 1/4}$	$\frac{\eta}{(e+\mathcal{P})\tau} \propto \tau^{2 \div 5/4}$

Table 2. Dependence of the hydrodynamic expansion parameter $\eta/[(e + \mathcal{P})\tau]$ as a function of time for two different functional forms for η ($\eta \propto T$ and $\eta \propto T^3$) and two expansion types (1D and 3D). A range of powers is given; the first power corresponds to ideal hydrodynamics and the second power corresponds to an estimate of non-equilibrium evolution.

expansion also becomes three dimensional. The system then enters the lower right corner of Table 2 and very quickly the nucleus-nucleus collision starts to break up. We note that it is necessary to introduce some scale into the problem in order to see this freezeout process. For a conformal liquid with $\eta \propto T^3$ the system never freezes out even for a 3D expansion. This can be seen by looking at the upper-right corner of the table and noting that the hydrodynamic expansion parameter behaves as

$$\frac{\eta}{(e + \mathcal{P})\tau} \propto \left(\frac{1}{\tau}\right)^{0 \div 1/4}, \quad (67)$$

and therefore approaches a constant (or slowly equilibrates) at late times. From this discussion we see that the temperature dependence of the shear viscosity is ultimately responsible for setting the duration of the hydrodynamic expansion.

4.6. *Second Order Hydrodynamics*

In the previous sections we developed the first order theory of relativistic viscous hydrodynamics. In the first-order theory there are reported instabilities which are associated with the gradient expansion⁸⁵. Specifically, in the first-order theory the stress tensor is instantly specified by the constituent relation and this leads to acausal propagation⁸⁶ and ultimately the instability. Nevertheless, it was generally understood that one could write down any relaxation model which conserved energy and momentum and which included some notion of entropy, and the results of such a model would be indistinguishable from the Navier Stokes equations^{87,88,89}. Many hydrodynamic models were written down^{90,91,92,93,94} starting with a phenomenological model by Israel and Stewart^{95,90} and Müller⁹⁶. For example in the authors own work the strategy was to write down a fluid model (based on Ref.⁹³) which relaxed on some time scale to the Navier Stokes equations, solve these model equations on the computer, and finally to verify that the results are independent of the details of the model¹⁰. Thus the goal was to solve the Navier Stokes equations and to estimate the effects of higher order terms.

Recently an important work by R. Baier, P. Romatschke, D. T. Son, A. O. Starinets and M. A. Stephanov (hereafter BRSSS) clarified and classified the nature of these higher order terms²⁵. An important impetus for this work came from the AdS/CFT correspondence^{25,28,97}. Many of the fluid models discussed

above were motivated by kinetic theory. However, in the strongly coupled $\mathcal{N} = 4$ plasma, kinetic theory is not applicable, and the precise meaning of these models was vague. BRSSS determined precisely in what sense these second order viscous equations are theories and in what sense they are models. Simultaneously the Tatta group completed the calculation of the second order transport coefficients in $\mathcal{N} = 4$ SYM theory and clarified the hydrodynamic nature of black branes in the process²⁸.

The spirit of the BRSSS analysis is the following:

- (1) Write the stress tensor as an expansion in all possible second order gradients of conserved charges and external fields which are allowed by the symmetries. The transport coefficients are the coefficients of this gradient expansion.
- (2) In this expansion temporal derivatives can be rewritten as spatial derivatives using lower order equations of motion.
- (3) The conservation laws $\partial_\mu T^{\mu\nu} = 0$ and the associated constituent relation dictates the dynamics of the conserved charges in the presence of the external field. By adjusting the transport coefficients, this dynamics will be able to reproduce all the retarded correlators of the microscopic theory.

In general, for a theory with conserved baryon number there are many terms. By focusing on a theory without baryon number and also assuming that the fluid is conformally invariant, the number of possible second order terms is relatively small. The classification of gradients in terms of their conformal transformation properties was very useful, both theoretically and phenomenologically. At a theoretical level there are a manageable number of terms to write down. At a phenomenological level the gradient expansion converges more rapidly when only those second order terms which are allowed by conformal invariance are included (see Section 6). Subsequently when additional conformal breaking terms are added, the conformal classification provides a useful estimate for the size of these terms, *i.e.* quantities that scale as $T_\mu^\mu = e - 3p$ should be estimated differently than those that scale as energy density itself. In retrospect, this classification is an “obvious” generalization of the first order Navier-Stokes equations.

Proceeding more technically, in analogy to the constituent relation of the Navier-Stokes theory Eq. (52), BRSSS determine that the possible forms of the gradient expansion in a conformal liquid are

$$\begin{aligned} \pi^{\mu\nu} = & -\eta\sigma^{\mu\nu} + \eta\tau_\pi \left[\langle D\sigma^{\mu\nu} \rangle + \frac{1}{d-1}\sigma^{\mu\nu}\partial \cdot u \right] \\ & + \lambda_1 \langle \sigma^\mu{}_\lambda \sigma^{\nu\lambda} \rangle + \lambda_2 \langle \sigma^\mu{}_\lambda \Omega^{\nu\lambda} \rangle + \lambda_3 \langle \Omega^\mu{}_\lambda \Omega^{\nu\lambda} \rangle, \end{aligned} \quad (68)$$

where the vorticity tensor is defined as

$$\Omega^{\mu\nu} = \frac{1}{2}\Delta^{\mu\alpha}\Delta^{\nu\beta}(\partial_\alpha u_\beta - \partial_\beta u_\alpha), \quad (69)$$

and $d = 4$ is the number of space-time dimensions. Conformal invariance forces a

particular combination of second derivatives to have a single coefficient

$$\tau_\pi \left[\langle D\sigma^{\mu\nu} \rangle + \frac{1}{d-1} \sigma^{\mu\nu} \partial \cdot u \right]. \quad (70)$$

The time derivative $D\sigma^{\mu\nu}$ may be expanded out using lower order equations of motion if desired. The constituent relation (Eq. (68)) and the conservation laws form the second order equations of motion of a conformal fluid. They are precisely analogous to the first order theory. As in the first order case, these equations are also acausal.

To circumvent this issue, BRSSS (following the spirit of earlier work by Israel and Stewart^{95,90} and Müller⁹⁶) promote the constituent relation to a dynamical equation for the viscous components of the stress tensor $\pi^{\mu\nu}$. Using the lower order relation $\pi^{\mu\nu} = -\eta\sigma^{\mu\nu}$, the (conformal) dependence of η on temperature $\eta \propto T^{d-1}$, and the ideal equation of motion Eq. (32), the following equation arises for $\pi^{\mu\nu}$

$$\begin{aligned} \pi^{\mu\nu} = & -\eta\sigma^{\mu\nu} - \tau_\pi \left[\langle D\pi^{\mu\nu} \rangle + \frac{d}{d-1} \pi^{\mu\nu} \nabla \cdot u \right] \\ & + \frac{\lambda_1}{\eta^2} \langle \pi^\mu{}_\lambda \pi^{\nu\lambda} \rangle - \frac{\lambda_2}{\eta} \langle \pi^\mu{}_\lambda \Omega^{\nu\lambda} \rangle + \lambda_3 \langle \Omega^\mu{}_\lambda \Omega^{\nu\lambda} \rangle. \end{aligned} \quad (71)$$

From a numerical perspective the resulting equation of motion is now first order in time derivatives, hyperbolic and causal. The modes in this (and similar) models have been studied in Refs.^{89,86,25}

Nevertheless it should be emphasized that the domain of validity of the resulting equations is still the same as Eq. (68), *i.e.* the hydrodynamic regime. Thus for instance the second order equations should be used in a regime where

$$|\pi^{\mu\nu} + \eta\sigma^{\mu\nu}| \ll |\eta\sigma^{\mu\nu}|.$$

Outside of this regime there is no guarantee that entropy production predicted by this model will be positive during the course of the evolution²⁵. It should also be emphasized that this is not a unique way to construct a hydrodynamic model which reduces to Eq. (68) in the long wavelength limit – see Ref.⁷² for an example discussed in these terms. What is guaranteed is that any conformal model or dynamics (such as conformal kinetic theory^{26,27} or the dynamics predicted by AdS/CFT^{25,28}) will be expressible in the long wavelength limit in terms of the gradient expansion given above.

There is an important distinction between the first and second order theories^{87,72,88}. In the first order theory, the ideal motion is damped, and there are corrections to the ideal motion of order the inverse Reynolds number

$$\text{Re}^{-1} \equiv \frac{\eta}{(e + \mathcal{P})L^2} \Delta t \sim \frac{\ell_{\text{mfp}}}{L} \frac{v_{\text{th}} \Delta t}{L}, \quad (72)$$

where L is the characteristic spatial dimension of the system, Δt is the time of observation, and v_{th} is a typical quasi-particle velocity. Thus for sufficiently long times the viscous corrections become large and must be resummed by solving the

Navier-Stokes equations to capture the damping of the fluid motion. Once this is done however, the remaining higher order terms (which are captured by the second order theory) are *uniformly* small and modify the Navier-Stokes solution by an amount of order

$$\ell_{\text{mfp}}^2/L^2.$$

Often this makes these higher order terms difficult to measure in normal laboratory liquids⁷².

For completeness we record the model equations which have been discussed in the heavy ion literature^{5,30,9,29}.

- (1) The first of these is the simplified Israel-Stuart equation,

$$\pi^{\mu\nu} = -\eta\sigma^{\mu\nu} - \tau_\pi \langle D\pi^{\mu\nu} \rangle. \quad (73)$$

Since the derivatives do not appear as the combination

$$\langle D\pi^{\mu\nu} \rangle + \frac{d}{d-1}\pi^{\mu\nu}\nabla \cdot u, \quad (74)$$

but rather involve $\langle D\pi^{\mu\nu} \rangle$ separately, this model does not respect conformal invariance.

- (2) The second model is the full Israel-Stewart equation which has the following form⁹⁸

$$\pi^{\mu\nu} = -\eta\sigma^{\mu\nu} - \tau_\pi \langle D\pi^{\mu\nu} \rangle + \frac{1}{2}\pi^{\mu\nu}\frac{\eta T}{\tau_\pi}\partial_\rho\left(\frac{\tau_\pi}{\eta T}u^\rho\right) + 2\tau_\pi\pi^{\alpha(\mu}\Omega^{\nu)\alpha}, \quad (75)$$

$$\rightarrow -\eta\sigma^{\mu\nu} - \tau_\pi\left[\langle D\pi^{\mu\nu} \rangle + \frac{d}{d-1}\pi^{\mu\nu}\nabla \cdot u\right] + 2\tau_\pi\pi^{\alpha(\mu}\Omega^{\nu)\alpha}. \quad (76)$$

In the last line we have used the conformal relation, $\eta T/\tau_\pi \propto T^{d+1}$ and equation of motion, $D(\ln T) = -1/(d-1)\nabla \cdot u$. The model is equivalent to taking $\lambda_1 = \lambda_3 = 0$ and $\lambda_2 = -2\eta\tau_\pi$.

There has been some effort to compute the coefficients of the gradient expansion both at strong and weak coupling. The gradient expansion in Eq. (68) implies that the relative size of the coefficients is $(\ell_{\text{mfp}}/L)^2$, and this is of order $[\eta/(e + \mathcal{P})]^2$ in a relativistic theory. The strong coupling results^{25,28} are listed in Table 4.6. At weak coupling, the results of kinetic calculations are also listed in the table²⁶ (see also Ref.²⁷). In kinetic theory the physics of these higher order terms stems from the streaming terms and the collision integrals^{26,25}. To first order in the gradients, the distribution is modified from its equilibrium form

$$n \rightarrow n + \delta f, \quad (77)$$

where $\delta f \propto p^i p^j \sigma_{ij}$ – see Section 5. Substituting this correction back into the Boltzmann equation

$$P^\mu \partial_\mu f = -C[f], \quad (78)$$

Quality	$\mathcal{N} = 4$ SYM	QCD Kinetic Theory	Relaxation Time
$\eta\tau_\pi$	$4 - 2 \ln(2) \simeq 2.61$	5.9 to 5.0 (due to g)	6
λ_1	2	5.2 to 4.1 (due to g)	6 ($\equiv \eta\tau_\pi$)
λ_2	$-4 \ln(2) \simeq -2.77$	-11.8 to -10 ($\equiv -2\eta\tau_\pi$)	-12 ($\equiv -2\eta\tau_\pi$)
λ_3	0	0	0

Table 3. Compilation of values of (rescaled) second order transport quantities ($\eta\tau_\pi, \lambda_1, \lambda_2, \lambda_3$). All numbers in this table should be *multiplied* by $\eta^2/(e + \mathcal{P})$. The complete strong coupling results are from an amalgamation of Ref.²⁵ and Ref.²⁸. The weak coupling results are from Ref.²⁶ and the relaxation time approximation was studied in Ref.²⁵ and clarified in Ref.²⁶. Hydrodynamic simulations of the heavy ion event are not sensitive to these values. In a theory where $\lambda_1 = \eta\tau_\pi$ the second order corrections to a viscous $0 + 1$ dimensional Bjorken evolution vanish.

leads to several terms which are responsible for the second order corrections to hydrodynamics. We enumerate these contributions:

- (1) The τ_π and λ_2 terms are the result of streaming of the first viscous correction $P^\mu \partial_\mu \delta f$ and do not involve the collision integral. The common origin of these terms ultimately explains the relation between them, $\lambda_2 = -2\eta\tau_\pi$.
- (2) The contribution to λ_1 (the visco-elastic $\pi\pi$ term) reflects the streaming $P^\mu \partial_\mu \delta f$ and the non-linearities of the collision integral, $C[\delta f]$.
- (3) Finally the vorticity-vorticity term does not appear on the LHS of the Boltzmann equation and therefore this term vanishes in kinetic theory^{25,27,26}. In the strong coupling limit the absence of a vorticity-vorticity coupling is not understood.

In the relaxation time approximation discussed in Section 5 (with $\tau_R \propto E_{\mathbf{p}}$) the coefficient τ_π is readily calculated with linearized kinetic theory for a massless gas^{25,26}

$$\eta\tau_\pi = 6 \frac{\eta^2}{e + \mathcal{P}}, \quad (79)$$

The kinetic theory relations $\lambda_2 = -2\eta\tau_\pi$ and $\lambda_3 = 0$ are respected for the same reasons as the full theory. Also in the relaxation time approximation one finds, $\lambda_1 = \eta\tau_\pi$. In the full kinetic theory the *difference* $\lambda_1 - \eta\tau_\pi$ reflects the deviation from the quadratic ansatz discussed Section 5, and to a much lesser extent the non-linearities of the collision integral. Nevertheless the relation $\lambda_1 = \eta\tau_\pi$ almost holds indicating the dominance of the streaming term. Overall the relaxation time approximation provides a good first estimate of these coefficients in kinetic theory. This is important because the second order corrections to a $0 + 1$ Bjorken expansion vanish if $\lambda_1 = \eta\tau_\pi$ – see below.

From a practical perspective a majority of simulations have used the full Israel-Stewart equations^{5,30,11} and treated τ_π as a free parameter, varying $[\eta/(e + \mathcal{P})\tau_\pi]$ down from the relaxation time value by a factor of two. While it is gratifying that higher order transport coefficients can be computed and classified, the final phenomenological results (see Section 6) are insensitive to the precise value of all second order terms for $\eta/s \lesssim 0.3$ ^{31,30,10}. Thus, the full hydrodynamic simulations corroborate the estimate given in Section 4.4 for the range of validity of hydrodynamics.

4.7. Summary

We have discussed various orders in the gradient expansion of hydrodynamics. Here we would like to summarize these results for a 0 + 1 dimensional Bjorken evolution. The equation of motion for the Bjorken expansion is

$$\frac{de}{d\tau} = -\frac{e + T^{zz}}{\tau}, \quad (80)$$

where $T^{zz} \equiv \tau^2 T^{\eta\eta}$ is the stress tensor at mid space-time rapidity, $\eta_s = 0$. The stress tensor through second order is^{13,25,31}

$$T^{zz} = \mathcal{P} - \frac{4}{3}\frac{\eta}{\tau} + (\lambda_1 - \eta\tau_\pi)\frac{8}{9\tau^2}. \quad (81)$$

Each additional term reflects one higher order in the hydrodynamic expansion parameter $[\eta/(e + p)\tau]$ discussed in Section 4.4. We have made use of the intermediate results

$$\sigma^{\mu\nu} = \text{diag}(\sigma^{\tau\tau}, \sigma^{xx}, \sigma^{yy}, \tau^2\sigma^{\eta\eta}) = \left(0, \frac{2}{3\tau}, \frac{2}{3\tau}, -\frac{4}{3\tau}\right), \quad (82)$$

and

$$\langle \sigma^{\mu\lambda}\sigma_{\lambda\nu} \rangle = \text{diag}\left(0, -\frac{4}{9\tau^2}, -\frac{4}{9\tau^2}, \frac{8}{9\tau^2}\right). \quad (83)$$

Notice in Eq. (81) that there is a cancellation between the relaxation terms $\sim \eta\tau_\pi D\sigma$ and the visco-elastic response³¹, $\lambda_1\sigma\sigma$. In kinetic theory the difference $\eta\tau_\pi - \lambda_1$ is determined primarily from the deviation of δf from the quadratic ansatz (see Section 5). Thus $\eta\tau_\pi$ is expected to be approximately equal to λ_1 due to the overall kinematics of the streaming term²⁶, $P^\mu\partial_\mu\delta f$. Examining Table 4.6 we see that for a relaxation time approximation $\eta\tau_\pi = \lambda_1$ and the second order corrections to a 0 + 1 Bjorken expansion of a conformally invariant fluid vanish! This cancellation is partially present for the full kinetic theory and for the strongly interacting theory.

Fig. 14 shows the how the different orders in Eq. (81) influence the evolution of the energy density for a conformally invariant equation of state ($\mathcal{P} = e/3 = sT/4$) and various values of η/s . For definiteness we have used the $\mathcal{N} = 4$ ratios for the second order transport coefficients but this makes little difference since only the

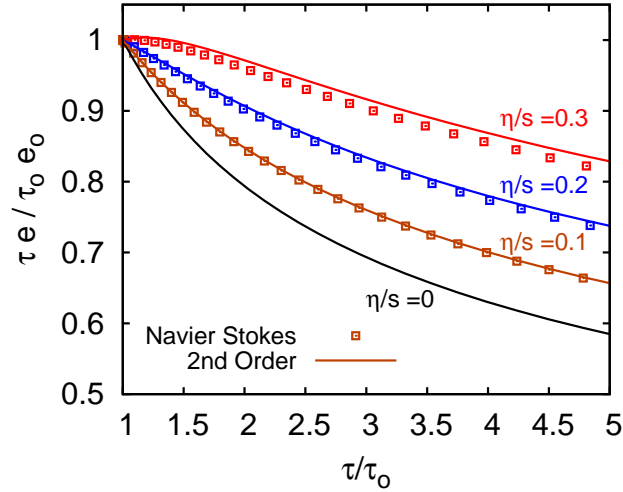


Fig. 14. The energy density ($\times\tau$) relative to the initial energy density ($\times\tau_0$) for a 0+1 dimensional Bjorken expansion. The temperature is $T_0 \simeq 300$ MeV and $\tau_0 \simeq 1$ fm, so that $1/\tau_0 T_0 \simeq 0.66$. The second order correction is smaller than expected due to a cancellation between the relaxation term $\sim \eta\tau_\pi D\sigma$ and the viscoelastic term³¹, $\sim \lambda_1\sigma\sigma$. In a relaxation time approximation the second order correction vanishes (see text).

combination $\lambda - \eta\tau_\pi$ matters – see Table 4.6. Finally we have used the estimates of Section 4.4 for the initial temperature T_0 and time τ_0

$$\frac{1}{\tau_0 T_0} = 0.66 \left(\frac{1 \text{ fm}}{\tau_0} \right) \left(\frac{300 \text{ MeV}}{T_0} \right).$$

Generally the effect of second order terms is small (due to the cancellation) and the value of the first order terms drive the correction to the ideal evolution.

5. Kinetic Theory Description

In Section 4 we discussed various aspects of viscous hydrodynamics as applied to heavy ion collisions. Since ultimately the experiments measure particles, there is a need to convert the hydrodynamic information into particle spectra. This section will provide an introduction to the matching between the kinetic and hydrodynamic descriptions. This will be important when comparing the hydrodynamic models to data in Section 6. In addition, since Section 3 discussed various calculations of the shear viscosity in QCD, this section we will sketch briefly how these kinetic calculations are performed. Good summaries of this set of steps are provided by Refs.^{99,73,100}.

In kinetic theory the spectrum of particles in a volume Σ is given by the Cooper-

Frye formula¹⁰¹

$$E \frac{d^3 N}{d^3 \mathbf{p}} = \frac{1}{(2\pi)^3} \int_{\Sigma} d\Sigma_{\mu} P^{\mu} f(-P \cdot u). \quad (84)$$

Note that when Σ is a three volume at fixed time, $d\Sigma_{\mu} = (dV, 0, 0, 0)$, and this formula reduces to the traditional result. Four vectors are denoted with capitol letters $P^{\mu} = (E_{\mathbf{p}}, \mathbf{p})$, and the equilibrium distribution function is denoted with

$$n(-P \cdot u) = \frac{1}{\exp(-P \cdot u/T) \pm 1}. \quad (85)$$

We will also use a suffix notation, $n_{\mathbf{p}} = n(-P \cdot U)$ and $f_{\mathbf{p}} = f(-P \cdot u)$. The distribution function obeys the Boltzmann equation

$$\partial_t f_{\mathbf{p}} + v_{\mathbf{p}} \cdot \partial_x f_{\mathbf{p}} = - \int_{234} \Gamma_{12 \rightarrow 34} (f_1 f_2 - f_3 f_4), \quad (86)$$

where $v_{\mathbf{p}} = \partial E_{\mathbf{p}} / \partial \mathbf{p} = \mathbf{p} / E_{\mathbf{p}}$, and we have assumed $2 \rightarrow 2$ scattering with classical statistics for simplicity, $f_{\mathbf{p}} = \exp(-E_{\mathbf{p}}/T)$. The momenta are labeled as $f_2 = f_{\mathbf{p}_2}$ and $f_1 = f_{\mathbf{p}_1}$ with $\mathbf{p}_1 \equiv \mathbf{p}$. The integral over the phase space is abbreviated

$$\int_{234} = \int \frac{d^3 \mathbf{p}_2}{(2\pi)^3} \frac{d^3 \mathbf{p}_3}{(2\pi)^3} \frac{d^3 \mathbf{p}_4}{(2\pi)^3}, \quad (87)$$

and the transition rate $\Gamma_{12 \rightarrow 34}$ for $2 \rightarrow 2$ scattering is related to the usual Lorentz invariant matrix element $|\mathcal{M}|^2$ by

$$\Gamma_{12 \rightarrow 34} = \frac{|\mathcal{M}|^2}{(2E_1)(2E_2)(2E_3)(2E_4)} (2\pi)^4 \delta^4(P_1 + P_2 - P_3 - P_4). \quad (88)$$

The generalization of what follows to a multi-component gas with quantum statistics is left to the references⁹⁹.

During a viscous evolution the spectrum will be modified from its ideal form

$$f = n_{\mathbf{p}} + \delta f_{\mathbf{p}}, \quad (89)$$

and this has important phenomenological consequences⁴. The modification of the distribution function depends on the details of the microscopic interactions. In a linear approximation the deviation is proportional to the strains and can be calculated in kinetic theory. When the most important strain is shear, the deviation δf is proportional σ_{ij} . Traditionally we parameterize the viscous correction to the distribution in the rest frame of the medium by^d $\chi(|\mathbf{p}|)$

$$\delta f_{\mathbf{p}} = -n_{\mathbf{p}} \chi(|\mathbf{p}|) \hat{\mathbf{p}}^i \hat{\mathbf{p}}^j \sigma_{ij}. \quad (90)$$

^d When quantum statistics are taken into account this should be written

$$\delta f_{\mathbf{p}} = -n_{\mathbf{p}} (1 \pm n_{\mathbf{p}}) \chi(|\mathbf{p}|) \hat{\mathbf{p}}^i \hat{\mathbf{p}}^j \sigma_{ij},$$

where the overall minus is introduced because in the Navier-Stokes theory $\pi^{\mu\nu} = -\eta \sigma^{\mu\nu}$

36 *Derek A. Teaney*

Then the stress tensor in the local rest frame is

$$T^{ij} = p\delta^{ij} - \eta\sigma^{ij} = \int \frac{d^3\mathbf{p}}{(2\pi)^3} \frac{p^i p^j}{E_{\mathbf{p}}} [n_{\mathbf{p}} + \delta f_{\mathbf{p}}]. \quad (91)$$

Substituting Eq. (90) for $\delta f_{\mathbf{p}}$ and using rotational symmetry we have

$$\eta = \frac{2}{15} \int \frac{d^3\mathbf{p}}{(2\pi)^3} \frac{p^2}{E_{\mathbf{p}}} \chi(|\mathbf{p}|) n_{\mathbf{p}}. \quad (92)$$

Thus we see that the form of the viscous correction to the distribution function determines the shear viscosity.

To calculate the transport coefficients the Boltzmann equation is analyzed in the rest frame of a particular location \mathbf{x}_o . In a neighborhood of this point the temperature and flow fields are

$$u^\mu(\mathbf{x}, t) \simeq (1, u^i(\mathbf{x}, t)), \quad T(\mathbf{x}, t) \simeq T_o + \delta T(\mathbf{x}, t), \quad (93)$$

where $u^i(\mathbf{x}_o, t) = \delta T(\mathbf{x}_o, t) = 0$. The equilibrium distribution function in this neighborhood is

$$n(-P \cdot u) \simeq n_{\mathbf{p}}^o + n_{\mathbf{p}}^o \left(\frac{E_{\mathbf{p}}}{T_o^2} \delta T(\mathbf{x}, t) + \frac{p^i u^i(\mathbf{x}, t)}{T_o} \right), \quad (94)$$

where we have used the short hand notation, $n_{\mathbf{p}}^o = \exp(-E_{\mathbf{p}}/T_o)$. We can now substitute the distribution function into the Boltzmann equation and find an equation for δf . The left hand side of the Boltzmann equation involves gradients, and therefore only the equilibrium distribution needs to be considered. Substituting Eq. (94) into the l.h.s. of Eq. (86), using the ideal equations of motion

$$\partial_t u^i = -\frac{\partial^i \mathcal{P}}{(e + \mathcal{P})}, \quad (95)$$

$$\partial_t e = -(e + \mathcal{P}) \partial_i u^i, \quad (96)$$

and several thermodynamic relationships

$$c_v = \frac{de}{dT}, \quad (97)$$

$$\frac{n}{e + \mathcal{P}} d(\mu/T) = \frac{1}{T(e + \mathcal{P})} d\mathcal{P} + d\left(\frac{1}{T}\right) = 0, \quad (98)$$

we find that^e

$$\partial_t f_e + v_{\mathbf{p}} \cdot \partial_{\mathbf{x}} f_e = \frac{n_{\mathbf{p}}}{E_{\mathbf{p}}} \left[\left(\frac{|\mathbf{p}|^2}{3T} - \frac{E_{\mathbf{p}}^2}{T} \frac{(e + \mathcal{P})}{T c_v} \right) \partial_i u^i + \frac{p^i p^j}{2T} \sigma_{ij} \right]. \quad (99)$$

The result is proportional to two strains $\partial_i u^i$ and σ_{ij} which are ultimately responsible for the bulk and shear viscosities respectively. For a massless conformal gas

^eWe have tacitly assumed that the dispersion curve $E(\mathbf{p})$ does not depend on the temperature. This is fine as long as we are not considering the bulk viscosity ⁷³.

we have $|\mathbf{p}|^2 = E_{\mathbf{p}}^2$, $Tc_v = 4e$ and $e + p = (4/3)e$. The result is that the term proportional to $\partial_i u^i$ vanishes and consequently the bulk viscosity is zero in this limit. Subsequently, we will consider only the modifications due to the shear viscosity and refer to Section 3 for a more complete discussion of bulk viscosity.

In Eq. (99), the l.h.s. of the Boltzmann equation is evaluated at the point \mathbf{x}_o . We also evaluate the r.h.s. of the Boltzmann equation at the point \mathbf{x}_o to linear order in δf

$$n_{\mathbf{p}}^o \frac{p^i p^j}{2TE_{\mathbf{p}}} \sigma_{ij} = - \int_{234} \Gamma_{12 \rightarrow 34} n_{\mathbf{p}}^o n_2^o \left[\frac{\delta f(\mathbf{p})}{n_{\mathbf{p}}^o} + \frac{\delta f_2}{n_2^o} - \frac{\delta f_3}{n_3^o} - \frac{\delta f_4}{n_4^o} \right]. \quad (100)$$

In writing this equation we have made use of the detailed balance relation

$$n_1 n_2 \Gamma_{12 \rightarrow 34} = n_3 n_4 \Gamma_{12 \rightarrow 34}. \quad (101)$$

Eq. (100) should be regarded as a matrix equation for the distribution function $\delta f(\mathbf{p})$. Although $\delta f(\mathbf{p})$ or $\chi(p)$ can be determined numerically by straight forward discretization and matrix inversion, a variational method is preferred in practice^{64,99}. After determining $\delta f(\mathbf{p})$ or $\chi(|\mathbf{p}|)$ the shear viscosity can be determined from Eq. (92).

Inverting the integral equation in Eq. (100) requires a detailed knowledge of the microscopic interactions. Lacking such detailed knowledge, one can resort to a relaxation time approximation, writing the Boltzmann equation as

$$\partial_t f + v_{\mathbf{p}} \cdot \partial_{\mathbf{x}} f = - \frac{1}{\tau_R(-P \cdot U)} \frac{(-P \cdot U)}{E_{\mathbf{p}}} \delta f, \quad (102)$$

where $\tau_R(-P \cdot U)$ is a momentum dependent relaxation time. In the local rest frame this reduces to

$$\partial_t f + v_{\mathbf{p}} \cdot \partial_{\mathbf{x}} f = - \frac{1}{\tau_R(E_{\mathbf{p}})} \delta f. \quad (103)$$

By fiat the correction to the distribution function is simple

$$\delta f = -n_{\mathbf{p}} \frac{\tau_R(E_{\mathbf{p}})}{2TE_{\mathbf{p}}} p^i p^j \sigma_{ij}. \quad (104)$$

First we consider the case where the relaxation time grows with energy

$$\tau_R(E_{\mathbf{p}}) = \text{Const} \times \frac{E_{\mathbf{p}}}{T} \quad \delta f = -\text{Const} \times n_{\mathbf{p}} \frac{p^i p^j}{2T^2} \sigma_{ij} \quad (105)$$

The form of this correction is known as the quadratic ansatz and was used by all hydrodynamic simulations so far^{5,10,31,30}. Substituting this form into Eq. (92) one determines that for a classical gas of arbitrary mass the constant is⁴

$$\text{Const} = \frac{\eta}{e + \mathcal{P}}, \quad \text{with} \quad \tau_R(E_{\mathbf{p}}) \propto E_{\mathbf{p}}. \quad (106)$$

For a Bose or Fermi gas we have the replacement $n_{\mathbf{p}} \rightarrow n_p(1 \pm n_p)$ and Eq. (106) is approximate holding at the few percent level. For a mixture of different classical particles with one *common* relaxation time Eq. (106) also holds. In practical

simulations this correction is written covariantly and the phenomenological field $\pi^{\mu\nu} = -\eta\sigma_{\mu\nu}$ is used, leading to the final result

$$\delta f = \frac{1}{2(e + \mathcal{P})T^2} P^\mu P^\nu \pi_{\mu\nu}. \quad (107)$$

The quadratic ansatz may seem arbitrary, but it is often a good model of collisional energy loss and weak scattering. For instance an analysis of the leading-log Boltzmann equation (along the lines of Eq. (100)) shows that the quadratic ansatz describes the full results to 10-15% accuracy⁹⁹. However, this agreement is in part an artifact of the leading-log, or soft scattering, approximation. For example, in the leading-log plasma the energy loss of a “high” p_T quark from the bath is given by¹⁰²

$$\frac{dp}{dt} = \left(N_c + \frac{N_f}{2} \right) \frac{C_F g^4 T^2}{24\pi} \log(T/m_D). \quad (108)$$

From this formula we see that the energy loss is constant at high momentum and therefore the relaxation time scales as $\tau_R \propto p$ in agreement with Eq. (105). In reality Eq. (108) is decidedly wrong at large momentum where radiative energy loss becomes increasingly significant and can shorten the relaxation time. Indeed when collinear radiation is included in the Boltzmann equation the quadratic ansatz becomes increasingly poor¹⁰³. In Section 6 we will consider a relaxation time which is independent of energy as an extreme alternative

$$\tau_R \propto \text{Const}, \quad (109)$$

and explore the phenomenological consequences of this ansatz.

As discussed in Section 6, the differential elliptic flow $v_2(p_T)$ is sensitive to the form of these corrections, while the integrated v_2 is constrained by the underlying hydrodynamic variables, and is largely independent of these details. This last remark should be regarded with caution as it has not been fully quantified.

6. Viscous Hydrodynamic Models of Heavy Ion Collisions

At this point we are in a position to discuss several viscous hydrodynamic models which have been used to confront the elliptic flow data. To initiate discussion, we show simulation results for $v_2(p_T)$ from Luzum and Romatschke in Fig. 15. Comparing the simulation to the “non-flow corrected” data for $p_T \lesssim 1.5$ GeV, we can estimate an allowed range for the shear viscosity, $\eta/s \approx 0.08 \leftrightarrow 0.16$. Below we will place this estimate in context by culling figures from related works.

A generic implementation of viscous hydrodynamics consists of several parts:

- (1) At an initial time τ_o the energy density and flow velocities are specified. For Glauber initial conditions, one takes for example

$$e(\tau_o, \mathbf{x}_\perp) \propto \frac{dN_{\text{coll}}}{dx dy}, \quad (110)$$

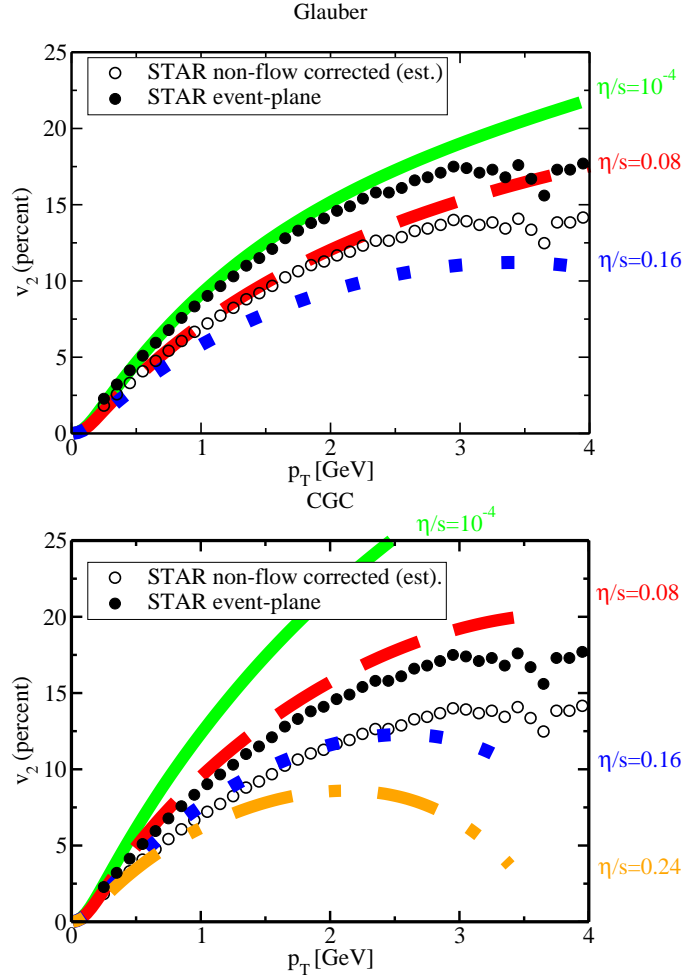


Fig. 15. Figure from Ref.³¹ which shows how elliptic flow depends on shear viscosity. The theory curves are most dependable for $p_T \lesssim 1.5$ GeV and should be compared to the “non-flow corrected” data. The Glauber and CGC initial conditions have different eccentricities as described in the text.

where the overall constant is adjusted to reproduce the multiplicity in the event. The simulations assume Bjorken boost invariance with the ansatz

$$e(\tau, \mathbf{x}_\perp, \eta) \equiv e(\tau, \mathbf{x}_\perp), \quad (111)$$

$$u^\mu(\tau, \mathbf{x}_\perp, \eta) = (u^\tau, u^x, u^y, u^\eta) = (u^\tau(\tau, \mathbf{x}_\perp), u^x(\tau, \mathbf{x}_\perp), u^y(\tau, \mathbf{x}_\perp), 0). \quad (112)$$

In cartesian coordinates $u^z = u^\tau \sinh(\eta_s)$ and $u^t = u^\tau \cosh(\eta_s)$. The calculations typically assume zero transverse flow velocity at the initial time τ_o

$$u^x(\tau_o, \mathbf{x}_\perp) = u^y(\tau_o, \mathbf{x}_\perp) = 0, \quad u^\tau(\tau_o, \mathbf{x}_\perp) = 1. \quad (113)$$

The strains are taken from the Navier stokes theory for example

$$\pi^{\mu\nu}(\tau_0, \mathbf{x}_\perp) = \text{diag}(\pi^{\tau\tau}, \pi^{xx}, \pi^{yy}, \tau^2 \pi^{\eta\eta}) = \left(0, \frac{2\eta}{3\tau}, \frac{2\eta}{3\tau}, -\frac{4\eta}{3\tau}\right), \quad (114)$$

and reflect the traceless character of shear stress.

- (2) The equations of motion are then solved. Viscosity modifies the hydrodynamic variables, T and u^μ , and also modifies off diagonal components of the stress tensor through the viscous corrections $\pi^{\mu\nu}$.
- (3) A “freezeout” condition is specified either by specifying a freezeout temperature or a kinetic condition. During the time evolution a freezeout surface is constructed. For instance the freezeout surface in Fig. 15 is the space-time three volume Σ where $T_{f0} \simeq 150$ MeV.
- (4) Finally, in order to compare to the data, particle spectra are computed by matching the hydrodynamic theory onto kinetic theory. Specifically, on the freezeout surface final particle spectra are computed using Eq. (125). Roughly speaking this “freezeout” procedure is equivalent to running the hydro up to a particular proper time τ_f or temperature T_f and declaring that the thermal spectrum of particles at that moment is the measured particle spectrum.

There are many issues associated with each of these items. The next subsections will discuss them one by one.

6.1. *Initial Conditions*

First we note that the hydrodynamic fields are initialized at a time $\tau_0 \simeq 1$ fm/c, which is arbitrary to a certain extent. Fortunately, both in kinetic theory and hydrodynamics the final results are not particularly sensitive this value^{104,31}. Also, all of the current simulations have assumed Bjorken boost invariance. While this assumption should be relaxed, past experience with ideal hydrodynamics shows that the mid-rapidity elliptic flow is not substantially modified¹⁸. Above we have discussed one possible initialization of the hydro which makes the energy density proportional to the number of binary collisions, *e.g.* the Glauber curves of Fig. 15. Another reasonable option is to make the entropy proportional to the number of participants¹⁰

$$s(\tau_0, \mathbf{x}_\perp) \propto \frac{dN_p}{dx dy}. \quad (115)$$

As a limit one can take the CGC model discussed in Section 2. Finally it is generally assumed that the initial transverse flow is zero

$$u_x(\tau_0, \mathbf{x}_\perp) = u_y(\tau_0, \mathbf{x}_\perp) = 0. \quad (116)$$

This assumption should probably lifted in future calculations and a more reasonable (but still small) estimate is given in Ref.¹⁰⁵.

Examining Fig. 15 and Fig. 7 we see see that there is a significant and predictable linear dependence on the eccentricity. When extracting the shear viscosity

from the data, this uncertainty in the eccentricity leads to a factor of two uncertainty in the final results for the shear viscosity. As emphasized in Section 2, the CGC model should be thought of as an upper limit to the anisotropy that can be produced in the initial state. Therefore, the uncertainty in η/s is probably not as large as dispersion in the curves would indicate. In ideal hydrodynamics, the spread in $v_2(p_T)$ resulting from the different initializations specified by Eq. (115) and Eq. (110) was studied¹⁰⁶, and is small compared to the difference between the Glauber and CGC curves in Fig. 15.

Once the initial conditions for the temperature and the flow velocities are specified, the off diagonal components of the stress tensor $\pi^{\mu\nu}$ are determined by the spatial gradients in T and u^μ . To second order this is given by Eq. (68) and there is no ambiguity in this result. Time derivatives may be replaced with spatial derivatives using lower order equations of motion to second order accuracy. In the phenomenological theory $\pi^{\mu\nu}$ is promoted to a dynamical variable. Clearly the appropriate initial condition for this variable is something which deviates from $-\eta\sigma^{\mu\nu}$ by second order terms. However, the extreme choice $\pi^{\mu\nu} = 0$ was studied to estimate how initial non-equilibrium effects could alter the final results. This is just an estimate since the relaxation of these fields far from equilibrium is not well captured by hydrodynamics. On the other hand, comparisons with full kinetic theory simulations show that the Israel-Stewart model does surprisingly well at reproducing the relaxation dynamics of the full simulation²⁹. From a practical perspective, even with this extreme choice $\pi^{\mu\nu} = 0$, the stress tensor relaxes to the expected form $\pi^{\mu\nu} = -\eta\sigma^{\mu\nu}$ relatively quickly. The result is that $v_2(p_T)$ is insensitive to the different initializations of $\pi^{\mu\nu}$. This can be seen clearly from Fig. 16.

6.2. Corrections to the Hydrodynamic Flow

Once the initial conditions are specified, the equations of motion can be solved. First we address the size of the viscous corrections to the temperature and flow velocities. The magnitude of the viscous corrections depends on the size of the system and the shear viscosity. Fig. 17 shows a typical result for the AuAu system. As seen from the figure the effect of viscosity on the temperature and flow velocities is relatively small, of order $\sim 15\%$ for $\eta/s \simeq 0.2$.

An explanation for this result is the following¹⁰⁷: In the first moments of the collision the system is expanding in the longitudinal direction and the pressure in the longitudinal directions is reduced

$$\tau^2 T^{\eta\eta} = \mathcal{P} - \frac{4}{3} \frac{\eta}{\tau}. \quad (117)$$

At first sight, this means that the system cools more slowly and indeed this is initially true. However, since the shear tensor is traceless there is an increase in the transverse pressure which is uniform in all directions

$$T^{xx} = T^{yy} = \mathcal{P} + \frac{2}{3} \frac{\eta}{\tau}, \quad (118)$$

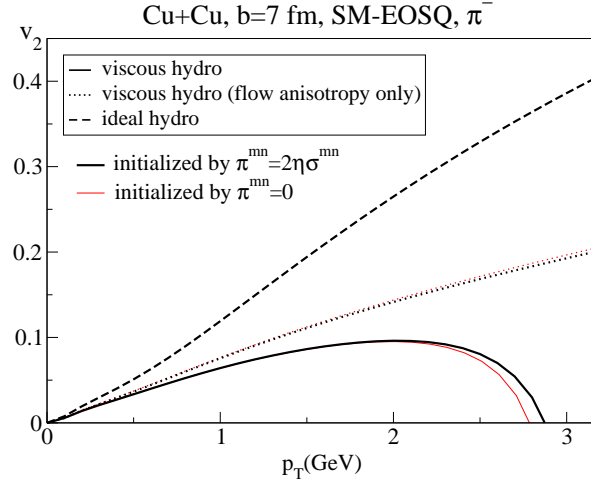


Fig. 16. Figure from Ref.⁹ studying the independence of the final results on the initialization of $\pi^{\mu\nu}$. Note that due to different metric and symmetrization conventions the Navier Stokes limit is $2\eta\sigma^{mn}$ rather than $-\eta\sigma^{\mu\nu}$ adopted here.

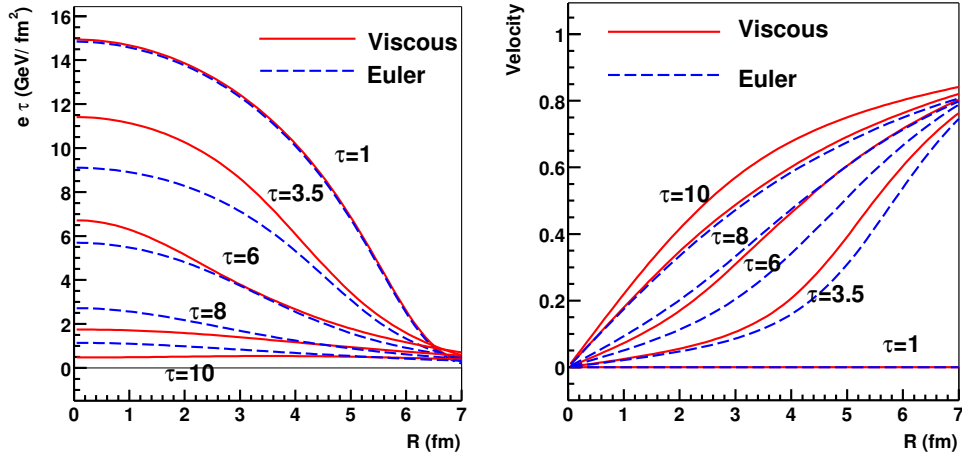


Fig. 17. A central AuAu simulation with an ideal gas equation of state $p = e/3$ and $\eta/s = 0.2$ which compares the viscous and Euler evolution¹⁰⁷. The left figure shows the energy density ($\times\tau$) for different times. The right figure shows the velocity for different times.

and which ultimately increases the radial flow. Since the radial flow is larger in the viscous case, the system ultimately cools faster.

Having discussed the dependence of T and u^μ , we turn to a quantity which largely dictates the final elliptic flow – the momentum anisotropy⁸¹. The momen-

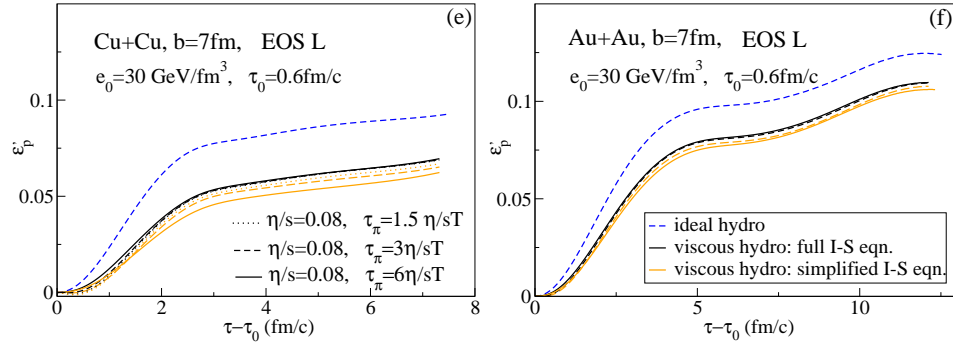


Fig. 18. Figure from Ref.³⁰ comparing the development of the flow anisotropy e'_p (Eq. (119)) in viscous hydrodynamics relative to the ideal hydrodynamics. The lower band of curves are all representative of viscous hydro and differ only in how the second order corrections are implemented. The anisotropy differs from ideal hydro because the anisotropy involves the viscous difference, $\Pi^{xx} - \Pi^{yy}$.

tum anisotropy is defined as^f

$$e'_p = \frac{\langle T^{xx} - T^{yy} \rangle}{\langle T^{xx} + T^{yy} \rangle} = \frac{\int d^2 \mathbf{x}_\perp (T^{xx} - T^{yy})}{\int d^2 \mathbf{x}_\perp (T^{xx} + T^{yy})}. \quad (119)$$

Fig. 18 illustrates how this momentum anisotropy increases as a function of time in the CuCu and AuAu systems. Although the flow fields $T(\mathbf{x}_\perp, \tau)$ and $u^\mu(\mathbf{x}_\perp, \tau)$ are quite similar between the ideal and viscous cases, the ideal anisotropy is significantly reduced by viscous effects. The reason for this reduction is because the viscous stress tensor anisotropy, $T^{xx} - T^{yy}$, involves the difference

$$\Pi^{xx} - \Pi^{yy},$$

in addition to the temperature and flow velocities. This additional term is ultimately responsible for the deviation of e'_p between the ideal and viscous hydrodynamic calculations. At later times there is some modification of e'_p , due to the flow itself, but this is dependent on freezeout. The deviation $\Delta\Pi = \Pi^{xx} - \Pi^{yy}$ will have important phenomenological consequences in determining the viscous correction to the elliptic flow spectrum.

^f Note there is a misprint in the original definition of e'_p in Ref.⁸¹. Eq. (3.2) of that work used a double bracket notation indicating an energy density weight which should only be a single bracket as above. This double bracket definition (rather than Eq. (119)) was used subsequently in Ref.¹⁰ which is why the associated curve differs from other recent works^{31,30}. Further the definition should perhaps include a factor of u^0 so that the integrals would be boost invariant, *i.e.* $\int d\Sigma_\mu u^\mu (T^{xx} - T^{yy}) = \tau \Delta \eta_s \int d^2 \mathbf{x} u^0 (T^{xx} - T^{yy})$. However, typically the integral is dominated near the center where $u^0 \simeq 1$. An alternative definition $S_{\text{hydro}}^{\mu\nu\rho}$ is suggested in Section 6.5.

6.3. Convergence of the Gradient Expansion

Fig. 18 also compares the simplified Israel-Stewart equation Eq. (74) to the full Israel-Stewart equation Eq. (75) as a function of the relaxation time parameter τ_π . The result supports much of the discussion given in Section 4.6. In the roughest approximation neither the simplified Israel-Stewart equation nor the full Israel-Stewart equation depend on the relaxation time parameter τ_π . When an ideal gas equation of state is used the dependence on τ_π is stronger especially for the simplified Israel-Stewart equation³⁰. Note also that the dependence on τ_π is stronger in the smaller CuCu system than in AuAu. However, in the conformally invariant full Israel-Stewart equation the dependence on τ_π is negligible, indicating that the result is quite close to the first order Navier Stokes theory. The more rapid convergence of the gradient expansion in conformally invariant fluids is a result of the fact that the derivatives in the conformal case come together as

$$\tau_\pi \left[\langle D\pi^{\mu\nu} \rangle + \frac{4}{3}\pi^{\mu\nu} \nabla \cdot u \right].$$

We have selected one figure out of many^{30,10,31}. The result of the analysis is that the flow fields and $v_2(p_T)$ are largely independent of the details of the second order terms at least for $\eta/s \lesssim 0.3$. For this range of parameters, hydrodynamics at RHIC is an internally consistent theory.

6.4. Kinetic Theory and Hydrodynamic Simulations

Clearly viscous hydrodynamics is an approximation which is not valid at early times and near the edge of the nucleus. This failure afflicts the current viscous calculations at a practical level right at the moment of initialization. For instance, the longitudinal pressure

$$T^{zz} \equiv \tau^2 T^{\eta\eta} = \mathcal{P} - \frac{4}{3} \frac{\eta}{\tau_0}, \quad (120)$$

eventually becomes negative near the edge of the nucleus indicating the need to transition to a kinetic description¹⁰⁸. (Note that $\mathcal{P} \propto T^4$ while $\eta \propto T^3$, so at sufficiently low temperatures the viscous term is always dominant regardless of the magnitude of η/s .) The current calculations simply limit the size of this correction through the phenomenological Israel-Stewart model. For example, one approach would be to take

$$\tau^2 T^{\eta\eta} = \mathcal{P} + \tau^2 \Pi^{\eta\eta}, \quad (121)$$

with

$$\tau^2 \Pi^{\eta\eta} = \begin{cases} -\frac{4}{3} \frac{\eta}{\tau_0} & \text{while } 4/3 \eta/\tau_0 < 0.9 \mathcal{P} \\ -0.9 \mathcal{P} & \text{otherwise} \end{cases}. \quad (122)$$

This ad-hoc fix is clearly not nice and points to the larger problem of freezeout which is difficult to address with hydrodynamics itself.

Freezeout is the colloquial term for the transition from a hydrodynamic to a kinetic regime and is impossible to separate cleanly from the viscosity itself in a realistic nucleus-nucleus collision. Clearly as the shear viscosity is made smaller and smaller, a larger and larger space time volume is described by hydrodynamics. To estimate the size of the relevant space time region we remark that hydrodynamics is valid when the relaxation time τ_R is much smaller than the inverse expansion rate, $\tau_R \partial_\mu u^\mu \ll 1$. Therefore, in the simulations one can estimate the region of validity by monitoring the expansion rate relative to the relaxation time^{109,110}. Specifically, freezeout is signaled when

$$\frac{\eta}{\mathcal{P}} \partial_\mu u^\mu \sim \frac{1}{2}. \quad (123)$$

This combination of parameters can be motivated from the kinetic theory estimates¹¹¹. The pressure is $\mathcal{P} \sim e \langle v_{\text{th}}^2 \rangle$, with $\langle v_{\text{th}}^2 \rangle$ the typical quasi-particle velocity. The viscosity is of order $\eta \sim e \langle v_{\text{th}}^2 \rangle \tau_R$ with τ_R the relaxation time. Thus hydrodynamics breaks down when

$$\frac{\eta}{\mathcal{P}} \partial_\mu u^\mu \sim \tau_R \partial_\mu u^\mu \sim \frac{1}{2}. \quad (124)$$

Fig. 19 estimates the space-time region described by viscous hydrodynamics. Examining this figure we see that the time duration of the hydrodynamic regime is a relatively strong function of η/s at least for a conformal gas. In reality the behavior of the shear viscosity near the transition region will control when the hydrodynamics will end.

Clearly the surface to volume ratio in Fig. 19 is not very small. Hydrodynamics is a terrible approximation near the edge. There is a need for a model which smoothly transitions from the hydrodynamic regime in the center to a kinetic or free streaming regime at the edge. Near the phase transition kinetic theory may not be a good model for QCD, but it has the virtue that it gracefully implements this hydro to kinetic transition. Although the interactions and the quasi-particle picture of kinetic theory may be decidedly incorrect, this is unimportant in the hydrodynamic regime. In the hydrodynamic regime the only properties that determine the evolution of the system are the equation of state, $\mathcal{P}(e)$, and the shear viscosity and bulk viscosities, $\eta(e)$ and $\zeta(e)$. In the sense that kinetic theory provides a reasonable guess as to how the surface to volume ratio influences the forward evolution, these models can be used to estimate the shear viscosity and the estimate may be more reliable than the hydrodynamic models. A priori one should demand that the kinetic models have the same equation of state and the same shear viscosity as expected from QCD, $\eta \propto T^3$. For instance in a kinetic model of massless particles with a constant cross section σ_o (such as studied in Ref.^{8,34,29}) the shear viscosity scales as $\eta \propto T/\sigma_o$. This difference with QCD should be kept in mind when extracting conclusions about the heavy ion reaction. Further, many transport models conserve particle number, which is an additional conservation law not inherent to QCD; this also changes the dynamics. Keeping these reservations in mind we examine Fig. 20 from Ref.¹¹. This

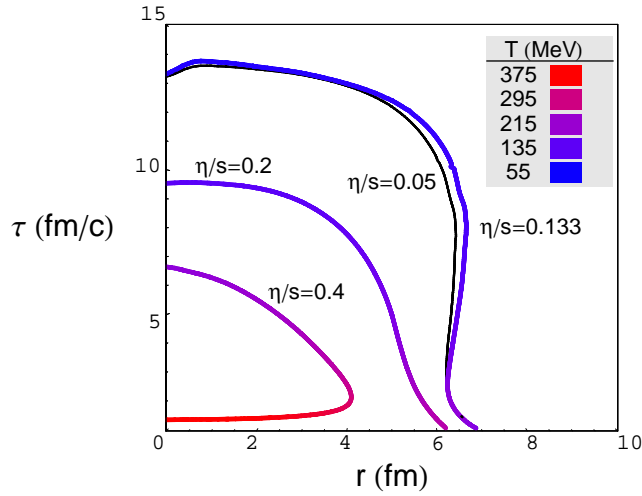


Fig. 19. This figure estimates for a conformal gas with equation of state $p = e/3$ and constant η/s the space time region described by viscous hydrodynamics¹⁰. The contours are where $(\eta/\mathcal{P}) \partial_\mu u^\mu = 0.6$ for different values of η/s . For the smallest value $\eta/s = 0.05$ the system freezes out at a time of order ~ 40 fm. This unrealistically long time reflects the conformal nature of the gas as discussed in Section 4.5. For comparison we have shown the $(\eta/\mathcal{P}) \partial_\mu u^\mu = 0.225$ contour for $\eta/s = 0.05$.

figure shows a promising comparison between kinetic theory with a constant cross section ($\sigma_\sigma = \text{Const}$) and a viscous hydrodynamic calculation with $\eta \propto T/\sigma_\sigma$. The case with $\sigma \propto \tau^{2/3}$ will not be discussed in this review, but is an attempt to mimic a fluid which has $\eta \propto T^3$.

What is exciting about this figure is the fact that the hydrodynamic conclusions are largely supported by the results of a similar kinetic theory. This gives considerable confidence that surface to volume effects are small enough that the hydrodynamic conclusions presented in Fig. 15 are largely unchanged by particles escaping from the central region. More formally, the opacity is large enough to support hydrodynamics.

There have been other kinetic calculations which are working towards extracting η/s from the heavy ion data^{12,32,33}. In particular Refs.^{7,6,112,113} used a kinetic theory implementation of $2 \rightarrow 2$ and $2 \rightarrow 3$ interactions motivated by weak coupling QCD³³. The simulation also calculates the Debye scale self consistently, *i.e.* in equilibrium one sets $m_D^2 \propto g^2 T^2$ and T changes with time. Out of equilibrium this mass scale m_D is determined from the momentum distribution of particles. Consequently this model respects the symmetry properties of high temperature QCD, *i.e.* the model has $\eta \propto T^3$ and does not conserve particle number. For the

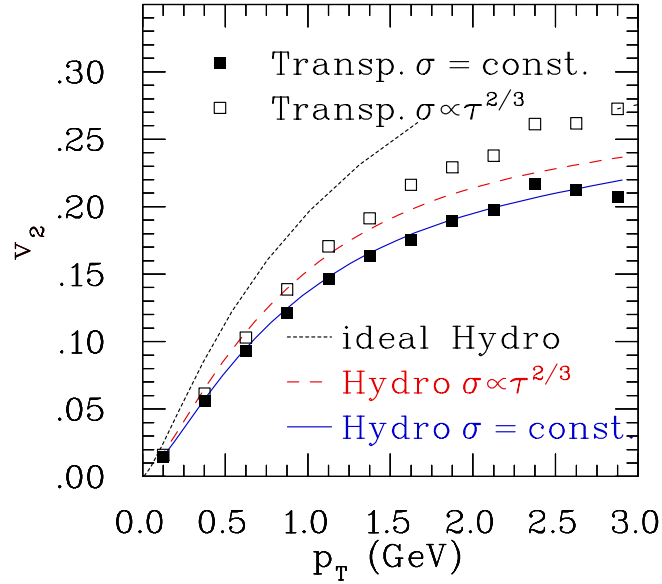


Fig. 20. Elliptic flow from Ref.¹¹ for a massless classical gas with a constant cross section in kinetic theory (Transp. $\sigma = \text{const.}$) and viscous hydrodynamics (Hydro $\sigma = \text{const.}$). The $\sigma \propto \tau^{2/3}$ case is not discussed in this review but is an effort to simulate a gas with $\eta \propto T^3$.

model parameter $\alpha_s = 0.3 \leftrightarrow 0.5$ (which is only schematically related to the running coupling) the shear to entropy ratio is $\eta/s = 0.16 \leftrightarrow 0.08$ ^{113,112}. The model (known as BAMPS) is conformal and never freezes out as discussed in Section 4.5. The current implementation of BAMPS simply stops the kinetic evolution when the energy density reaches a critical value, $e_c \simeq 0.6 \leftrightarrow 1.0 \text{ GeV/fm}^3$. This is an abrupt way to introduce a needed scale into the problem and schematically approximates the rapid variation of the shear viscosity in this energy density range. Fig. 21 shows the time development of elliptic flow in this model which can reproduce the observed flow only for $\eta/s = 0.16 \leftrightarrow 0.08$. The time development of v_2 seen in Fig. 21 shows that it is very difficult to separate precisely the shear viscosity in the initial stage from the freezeout process controlled by e_c .

Clearly the transition from a hydrodynamic regime to a kinetic regime is important to clarify in the future. In the meantime most hydrodynamic groups have invoked an ad-hoc freezeout prescription. In Refs.^{5,31,30,9} the hydrodynamic codes were run until a typical freezeout temperature, $T_{\text{fo}} \simeq 150 \text{ MeV}$. Technically the freezeout surface is constructed by marching forward in time and triangulating the space-time surface with constant temperature. In Ref.¹¹ a surface of constant particle density was chosen $n \simeq 0.365/\text{fm}^3$, and in Ref.¹⁰ the chosen surface was motivated by the kinetic condition in Eq. (123). Ideally this could be improved by dynamically coupling the hydrodynamic evolution to a kinetic description

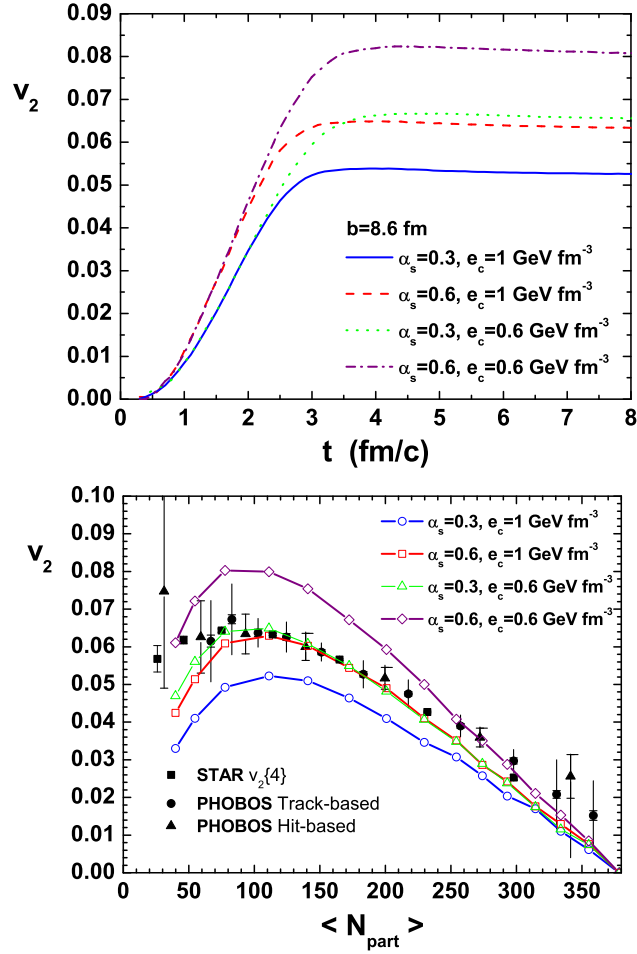


Fig. 21. (Top) The development of elliptic flow v_2 as a function of time in the BAMPS model⁷. (Bottom) The final elliptic flow as a function of centrality. The shear viscosity to entropy ratio η/s corresponding to the model parameter $\alpha_s = 0.3 \leftrightarrow 0.6$ was estimated in Ref.^{113,112} and is $\eta/s = 0.16 \leftrightarrow 0.08$. The evolution is stopped when the energy density reaches a critical value of e_c .

or by simulating the entire event with a kinetic model which closely realizes the equation of state and transport coefficients used in the hydrodynamic simulations.

6.5. Particle Spectra

Finally we turn to the particle spectra in viscous hydrodynamics. Ideally the system would evolve through the approximate phase transition down to sufficiently low temperatures where the dynamics could be described either with viscous hy-

drodynamics or with the kinetic theory of a Hadron Resonance Gas (HRG). In reality this does not seem particularly likely since the system is already expanding three dimensionally and the scales are approximately fixed (see Section 4.5). The estimates of the shear viscosity to entropy ratio in a hadronic gas are reliable for $T \lesssim 130$ MeV and do not support this optimistic picture (see Section 3). It seems quite unlikely that there is equilibrium evolution in the HRG below a temperature of $T \simeq 150$ MeV. Clearly the dynamics is extremely complex during the quark-hadron transition which takes place for an energy density of $e \simeq 0.5 \leftrightarrow 1.2$ GeV/fm³. In this range, the temperature changes by only $\Delta T \simeq 20$ MeV. However, the hydrodynamic simulations evolve this complicated region for a significant period of time, $\tau \simeq 4$ fm \leftrightarrow 7 fm. This transition region can be seen from the inflection in the AuAu plots in Fig. 18.

The pragmatic approach to this complexity is to compute the quasi-particle spectrum of hadrons at a temperature of $T \simeq 150$ MeV. Since the HRG describes the QCD thermodynamics well, this pragmatism is fairly well motivated. The approach conserves energy and momentum and when viscous corrections are included also matches the strains across the transition. In ideal hydrodynamics simulations the subsequent evolution of the hadrons has been followed with hadronic cascade models^{22,19,18}. The result of these hybrid models is that the hadronic rescattering is essentially unimportant for the $v_2(p_T)$ observables presented here.

Technically, the procedure is the following: along the freezeout surface the spectrum of particles is computed with the Cooper-Frye formula

$$E \frac{dN^a}{d^3\mathbf{p}} = \frac{d_a}{(2\pi)^3} \int_{\Sigma} d\Sigma_{\mu} P^{\mu} f^a(-P \cdot u/T), \quad (125)$$

where a labels the particle species, the distribution function is,

$$f^a(-P \cdot u) = n^a(-P \cdot u/T) + \delta f^a(-P \cdot u/T), \quad (126)$$

and d_a labels the spin-isospin degeneracy factor for each particle included (see Section 5). In practice, the Boltzmann approximation is often sufficient. In Ref.³¹ all particles were included up to mass of $m_{\text{res}} < 2.0$ GeV and then subsequently decayed. In other works a simple single species gas was used to study various aspects of viscous hydrodynamics divorced from this complex reality^{10,11}.

All of the viscous models used the quadratic ansatz discussed in Section 5, writing the change to the distribution function of the a -th particle type as

$$f^a \rightarrow n^a + \delta f^a, \quad (127)$$

with δf^a given by

$$\delta f^a = \frac{1}{2(e + \mathcal{P})T^2} n^a (1 \pm n^a) P^{\mu} P^{\nu} \pi_{\mu\nu}. \quad (128)$$

Before continuing we review the elements that go into a complete hydrodynamic calculation. First initial conditions are specified (see Section 6.1); then the equations are solved with the viscous term (see Section 6.2); after this a freezeout surface

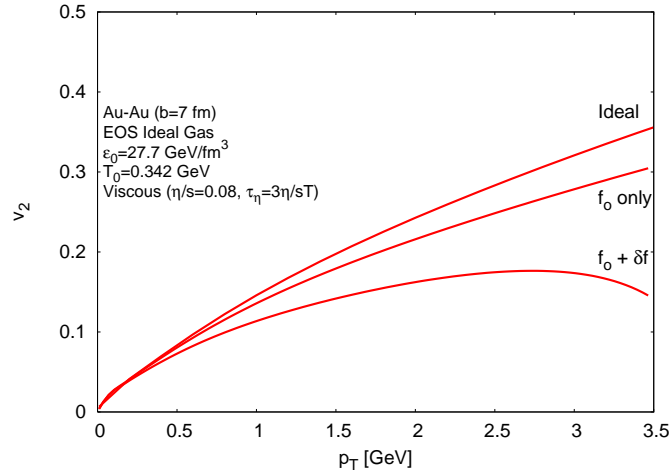


Fig. 22. $v_2(p_T)$ based on Refs.^{10,114} showing the $v_2(p_T)$ with $(f_o + \delta f)$ and without $(f_o \text{ only})$ the viscous modification of the distribution function. The result depends to a certain extent on freezeout and the freezeout temperature here is $T_{fo} = 130 \text{ MeV}$.

is specified (see Section 6.4 for the limitations of this); finally we compute spectra using Eq. (125) and Eq. (128). This particle spectra can ultimately be compared to the observed elliptic flow. With this oversight we take a more nuanced look at Fig. 15.

To separate the viscous modifications of the flow variables (T and u^μ) and the viscous modifications of the distribution function, we turn to Fig. 22. Examining this figure we see that a significant part of the corrections due to the shear viscosity are from the distribution function rather than the flow. Although the magnitude of the flow modifications depends on the details of freezeout, this dependence on δf is the typical and somewhat distressing result. We emphasize however that it is inconsistent to drop the modifications due to δf . The result of dropping the δf means that the energy and momentum of the local fluid cell $T^{\mu\nu}u_\nu$ is matched by the particle content, but the off diagonal strains $\pi^{\mu\nu}$ are not reproduced. The assumption underlying the comparison of viscous hydrodynamics to data is that the form of these off diagonal strains is largely unmodified from the Navier Stokes limit during the freezeout process. As the particles are “freezing out” this is a reasonable assumption. However, since these strains are only partially constrained by conservation laws, this assumption needs to be tested against kinetic codes as already emphasized above. This freezeout problem is clearly an obstacle to a reliable extraction of η/s from the data.

Although the dependence on δf in $v_2(p_T)$ is undesirable, the viscous modifications of the *integrated* elliptic flow v_2 largely reflects the modifications to the stress tensor itself. The observation is that the stress anisotropy e'_p (see Eq. (119))

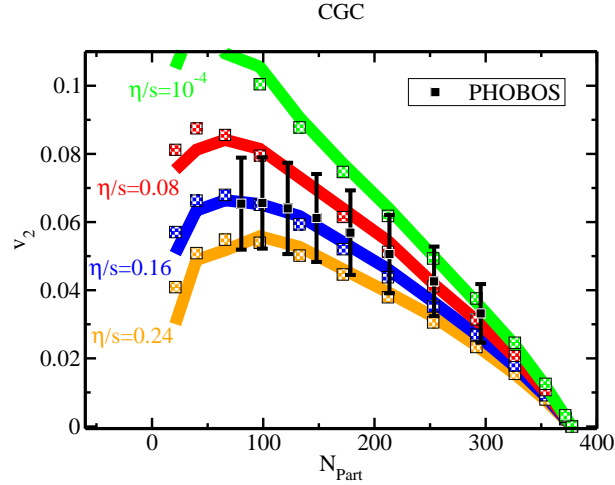


Fig. 23. Dependence of elliptic flow versus some centrality from Ref.³¹. The lines show the results of viscous hydrodynamics and the colored squares show the anisotropy of the stress tensor $0.5 e'_p$ (see Eq. (119)) for different values of η/s . The sensitivity to the quadratic ansatz is estimated in the text and corresponds to half the difference between the red ($\eta/s = 0.08$) and blue ($\eta/s = 0.16$) curves. The heuristic rule $v_2 \simeq 0.5 e'_p$ is motivated in the text.

determines the average flow according to a simple rule of thumb^{81,31}

$$v_2 \simeq \frac{1}{2} e'_p. \quad (129)$$

Fig. 23 shows e'_p and v_2 as a function of centrality. The figure supports this rule and suggests that sufficiently integrated predictions from hydrodynamics do not depend on the detailed form of the viscous distribution.

To corroborate this conclusion we turn to an analysis originally presented by Ollitrault¹⁶ and subsequently generalized to the viscous case^{10,115}. First we parameterize the single particle spectrum dN/dp_T with an exponential and $v_2(p_T)$ as linearly rising, *i.e.*

$$\frac{1}{p_T} \frac{dN}{dp_T} \simeq C e^{-p_T/T}, \quad \text{and} \quad v_2 \propto p_T. \quad (130)$$

With this form one finds quite generally that the p_T^2 weighted elliptic flow is twice the average v_2

$$2v_2 \simeq A_2 \equiv \frac{\langle p_x^2 - p_y^2 \rangle}{\langle p_x^2 + p_y^2 \rangle}. \quad (131)$$

The p_T^2 weighted elliptic flow has a much closer relationship to the underlying hydrodynamic variables. Indeed we will show how this simple rule of thumb arises and that it is largely independent of the details of δf .

52 *Derek A. Teaney*

To this end, we evaluate the sphericity tensor which will have a simple relationship to A_2

$$S^{\mu\nu\rho} = S_I^{\mu\nu\rho} + S_V^{\mu\nu\rho} = \int \frac{d^3\mathbf{p}}{(2\pi)^3 E_{\mathbf{p}}} P^\mu P^\nu P^\rho [n(-P \cdot u) + \delta f(-P \cdot u)] \quad (132)$$

Then using the Cooper-Frye formula (with $d\Sigma_\mu = (\tau d\eta_s d^2\mathbf{x}_\perp, 0, 0, 0)$) the asymmetry at any given moment in proper time is

$$A_2 = \frac{\int d^2\mathbf{x}_\perp (S^{0xx} - S^{0yy})}{\int d^2\mathbf{x}_\perp (S^{0xx} + S^{0yy})}. \quad (133)$$

The sphericity tensor consists of an ideal piece and a viscous piece

$$f \rightarrow n + \delta f, \quad S^{\mu\nu\rho} \rightarrow S_I^{\mu\nu\rho} + S_V^{\mu\nu\rho}. \quad (134)$$

First we consider the ideal piece and work in a classical massless gas approximation for ultimate simplicity. The tensor is a third rank symmetric tensor and can be decomposed as

$$S_I^{\mu\nu\rho} = A(T)u^\mu u^\nu u^\rho + B(T)(u^\mu g^{\nu\rho} + \text{perms}). \quad (135)$$

Here $A(T)$ and $B(T)$ are thermodynamic functions and are given by

$$\frac{A}{6} = B = \int \frac{d^3\mathbf{p}}{(2\pi)^3} \frac{p^2}{3} n_{\mathbf{p}} = (e + \mathcal{P})T. \quad (136)$$

For Bose and Fermi gases this relation between $A(T)$, $B(T)$, and the enthalpy is approximate. Thus the ideal piece of the sphericity tensor is largely constrained by thermodynamic functions. The viscous piece is largely constrained by the shear viscosity. As discussed in Section 5 we parameterize the δf with $\chi(p)$

$$\delta f = -n_{\mathbf{p}} \frac{\chi(p)}{(P \cdot U)^2} P^\mu P^\nu \sigma_{\mu\nu}. \quad (137)$$

While the precise form of the viscous correction $\chi(p)$ depends on the details of the microscopic interactions, it is constrained by the shear viscosity

$$\eta = \frac{2}{15} \int \frac{d^3\mathbf{p}}{(2\pi)^3} p \chi(p) n_{\mathbf{p}}. \quad (138)$$

Substituting the viscous parameterization into the definition of the sphericity we find

$$S^{0xx} = -C(T) [u^0 \sigma^{xx} + 2u^x \sigma^{x0}], \quad (139)$$

$$\simeq -C(T) u^0 \sigma^{xx}, \quad (140)$$

where $C(T)$ is

$$C(T) = \frac{2}{15} \int \frac{d^3\mathbf{p}}{(2\pi)^3} p^2 \chi(p) n_{\mathbf{p}}. \quad (141)$$

For simplicity we have assumed that the flow is somewhat non-relativistic so that $u^x \pi^{x0}$ is $O(v^2)$ compared to $u^0 \pi^{xx}$. To get a feeling for how sensitive the results are to the quadratic ansatz we will work with a definite functional form

$$\chi(p) = \text{Const} \times p^{2-\alpha}. \quad (142)$$

In a relaxation time approximation discussed in Section 5, $\alpha = 0$ corresponds to a relaxation time which increases with linearly p while $\alpha = 1$ corresponds to a relaxation time independent of p . Substituting this ansatz we find

$$C(T) \simeq (6 - \alpha)T\eta, \quad \text{where } 0 < \alpha < 1. \quad (143)$$

Having assembled the ingredients we can write down an approximate formula for A_2

$$A_2 \simeq \frac{\int d^2\mathbf{x}_\perp T u^0 [(e + \mathcal{P})(u^x u^x - u^y u^y) + (1 - \frac{\alpha}{6})(\pi^{xx} - \pi^{yy})]}{\int d^2\mathbf{x}_\perp T u^0 [(e + \mathcal{P})(u^x u^x + u^y u^y) + (e + \mathcal{P})/3 + (1 - \frac{\alpha}{6})(\pi^{xx} + \pi^{yy})]}, \quad (144)$$

with $0 < \alpha < 1$. This is the desired formula which expresses the observed elliptic flow in terms of the hydrodynamic variables. To reiterate, the coefficient α changes the functional form the viscous distribution function and $0 < \alpha < 1$ is a reasonable range — $\alpha = 0$ is the usual quadratic ansatz. It is useful to compare this formula to the definition of e'_p

$$e'_p = \frac{\int d^2\mathbf{x}_\perp [(e + \mathcal{P})(u^x u^x - u^y u^y) + (\pi^{xx} - \pi^{yy})]}{\int d^2\mathbf{x}_\perp [(e + \mathcal{P})(u^x u^x + u^y u^y) + 2\mathcal{P} + (\pi^{xx} + \pi^{yy})]}. \quad (145)$$

Thus while e'_p is not exactly equal to the A_2 of Eq. (144), it is close enough to explain the heuristic rule, $2v_2 \simeq e'_p$.

The overall symmetries and dimensions of the sphericity tensor suggests a definition for an analogous quantity in hydrodynamics

$$S_{\text{hydro}}^{\mu\nu\rho} = T \left[(e + \mathcal{P})u^\mu u^\nu u^\rho + \frac{1}{6}(e + \mathcal{P})(u^\mu g^{\nu\rho} + \text{perms}) + (u^\mu \pi^{\nu\rho} + \text{perms}) \right]. \quad (146)$$

In fact in a classical massless gas approximation with the quadratic ansatz, the analysis sketched above shows that

$$S_{\text{hydro}}^{\mu\nu\rho} = \frac{1}{6}S^{\mu\nu\rho}. \quad (147)$$

The important point for this review is that from Eq. (144) we see that the *integrated* elliptic flow is relatively insensitive to the quadratic form for the viscous distribution function. More specifically the uncertainty is $\sim 15\%$ of $A_2^{\text{ideal}} - A_2^{\text{viscous}}$, *i.e.* about half the difference between the blue ($\eta/s = 0.16$) and red curves ($\eta/s = 0.08$) in Fig. 23. However, the estimate shows that changing the quadratic ansatz will move the curves systematically higher increasing the preferred value of η/s to a certain extent. The quadratic ansatz (which has been used by all hydrodynamic simulations) can be a poor approximation when collinear emission processes are included in the Boltzmann description¹⁰³.

Clearly addressing more completely the uncertainties associated with the particle content and microscopic interactions in Fig. 23 is a task for the future. Nevertheless, it does seem that sufficiently integrated quantities will reflect rather directly the bulk properties of the hydrodynamic motion in a way that can be quantified.

7. Summary and Outlook

The elliptic flow data presented in Fig. 5 and Fig. 6 provide strong evidence for hydrodynamic evolution in a deconfined phase of QCD. It is difficult to think of other QCD based mechanisms which could explain the measured elliptic flow. This is because the nuclear geometry has a size $R_{Au} \sim 4$ fm, which is large compared to the momentum scales in the problem $p \sim 0.6$ GeV. Given this large size, the response of the nuclei to this initial geometry must develop over a relatively long time, $\tau \simeq 4$ fm/ c . Hydrodynamics is the appropriate framework to describe the collective motion over these long time scales.

We have discussed three advances which have corroborated the hydrodynamic interpretation of the flow. The first advance is experimental and a brief overview is provided in Section 2. These measurements now show quite clearly that the hydrodynamic response is from a deconfined phase (see Fig. 6). Furthermore, the measurements also show that the flow decreases in smaller systems in a systematic way (see Fig. 5).

The second advance is in viscous hydrodynamics. There has been important conceptual progress in understanding hydrodynamics beyond the Navier-Stokes order (see Section 4.6). The important result of this analysis (see Fig. 14) is that for a Bjorken expansion there are generic kinematic cancellations between the second order terms which reduce their relative importance. In fact in a $0 + 1D$ Bjorken expansion of a conformal gas in the relaxation time approximation, the second order corrections vanish, while in other more general kinetic theories the second order corrections almost vanish. This understanding of second order hydrodynamics has spurred additional progress in viscous simulations of the heavy ion event (see Section 6). It is satisfying that viscous hydrodynamics simulations are in better agreement with the data than ideal hydrodynamics and naturally explain several trends in the elliptic flow. For example, viscosity explains the fall off of v_2 at high momentum (see Fig. 22 and Fig. 5) and the fall off of v_2 in more peripheral collisions (see Fig. 5 and Fig. 23). Many of these trends were previously reproduced by transport models³ and it is exciting to see that they are now reproduced with a macroscopic approach.

The final advance has been in kinetic theory simulations. Kinetic theory simulations smoothly interpolate between the hydrodynamic regime and free streaming. Since hydrodynamics is universal (*i.e.* it only depends on $\mathcal{P}(e)$ and $\eta(e)$), the kinetic theory results can be used to estimate how still higher gradients would influence the hydrodynamic conclusions. Ideally the results of these simulations would be largely independent of the details of the interactions. The kinetic simulations have

demonstrated the ability to reproduce the viscous hydrodynamics (see Fig. 20)), validating the hydrodynamic assumption that the dynamics near the edge does not significantly influence the time development of elliptic flow. In addition, various advances have allowed these kinetic codes to simulate a fluid which does not conserve particle number and which has a shear viscosity, $\eta \propto T^3$ (see Fig. 21). Thus, the estimates of η/s from these simulations are complementary to the macroscopic approach, and must be accepted even if theoretical prejudice rejects the microscopic details.

Examining the figures in this review, we see that there is consensus between hydrodynamic and kinetic models on several points^{3,4,5,6,7,8,9,10,11,12}:

- Shear viscosity is needed to reproduce trends in the data. This consensus has yet to translate to an agreed upon lower bound on η/s but probably will in the not too distant future.
- It is impossible to reproduce the elliptic flow if the shear is too large:

$$\eta/s \gtrsim 0.4. \quad (148)$$

This bound is quite safe and has been found by all groups which have tried to reproduce the observed flow.

- The preferred value of η/s is (see Fig. 15 and Fig. 21)

$$\eta/s \simeq (1 \leftrightarrow 3) \times \frac{1}{4\pi}.$$

To reduce these constraints further several items need to be studied and quantified.

- At the end of the collision kinetic assumptions need to be made. The uncertainties involved with the particle content and the quadratic ansatz to the distribution need to be quantified to a much greater extent than has been done so far. The theoretical motivations and limitations of the quadratic ansatz have been discussed in Section 5. In Section 6.5 we have taken the nascent steps to quantify these uncertainties with an independent analysis of Fig. 23 due to Luzum and Romatschke.
- The nucleus-nucleus collision terminates as the system enters the transition region and starts expanding three dimensionally. Some estimates for this transition process have been given in Section 4.5. Clearly the transition region sets a very definite scale $e \simeq 0.6 \leftrightarrow 1.2 \text{ GeV/fm}^3$ which can not be ignored. It is difficult to separate the rapid $\eta(e)$ dependence in this region from the shear viscosity well into the QGP phase (See Fig. 21). This scale influences the dependence of v_2 on centrality and hampers an extraction of η/s from this size dependence. It will be important to categorize in a model independent way (*e.g.* $\eta(e)$) how this scale influences the final flow and the final estimates of η/s .

Finally, while this review has focused squarely on elliptic flow, the short transport time scales estimated here have implications for a large number of other observables – energy loss^{1,2}, the ridge and Mach cones^{116,117,118}, heavy quarks^{119,120},

and many more. Ultimately these observables will provide a more complete picture of strongly coupled dynamics near the QCD phase transition.

Acknowledgments

I gratefully acknowledge help from Raimond Snellings, Kevin Dusling, Paul Romatschke, Peter Petreczky, Denes Molnar, Guy Moore, Pasi Huovinen, Tetsufumi Hirano, Peter Steinberg, Ulrich Heinz, Thomas Schaefer, and Carsten Greiner. Any misstatements and errors reflect the shortcomings of the author. I also am grateful to the organizers and participants of the Nearly Perfect Fluids Workshop which clarified the appropriate content of this review. D.T. is supported by the U.S. Department of Energy under an OJI grant DE-FG02-08ER41540 and as a Sloan Fellow.

References

1. J. Adams *et al.* [STAR Collaboration], Nucl. Phys. A **757**, 102 (2005) [arXiv:nucl-ex/0501009].
2. K. Adcox *et al.* [PHENIX Collaboration], Nucl. Phys. A **757**, 184 (2005) [arXiv:nucl-ex/0410003].
3. D. Molnar and M. Gyulassy, Nucl. Phys. A **697**, 495 (2002) [Erratum-ibid. A **703**, 893 (2002)] [arXiv:nucl-th/0104073].
4. D. Teaney, Phys. Rev. C **68**, 034913 (2003) [arXiv:nucl-th/0301099].
5. P. Romatschke and U. Romatschke, Phys. Rev. Lett. **99**, 172301 (2007) [arXiv:0706.1522 [nucl-th]].
6. Z. Xu, C. Greiner and H. Stoecker, Phys. Rev. Lett. **101**, 082302 (2008) [arXiv:0711.0961 [nucl-th]].
7. Z. Xu and C. Greiner, Phys. Rev. C **79**, 014904 (2009) [arXiv:0811.2940 [hep-ph]].
8. H. J. Drescher, A. Dumitru, C. Gombeaud and J. Y. Ollitrault, Phys. Rev. C **76**, 024905 (2007) [arXiv:0704.3553 [nucl-th]].
9. H. Song and U. W. Heinz, Phys. Rev. C **77**, 064901 (2008) [arXiv:0712.3715 [nucl-th]].
10. K. Dusling and D. Teaney, Phys. Rev. C **77**, 034905 (2008) [arXiv:0710.5932 [nucl-th]].
11. D. Molnar and P. Huovinen, J. Phys. G **35**, 104125 (2008) [arXiv:0806.1367 [nucl-th]].
12. G. Ferini, M. Colonna, M. Di Toro and V. Greco, Phys. Lett. B **670**, 325 (2009) [arXiv:0805.4814 [nucl-th]].
13. P. Danielewicz and M. Gyulassy, Phys. Rev. D **31**, 53 (1985).
14. G. Policastro, D. T. Son and A. O. Starinets, Phys. Rev. Lett. **87**, 081601 (2001) [arXiv:hep-th/0104066].
15. P. Kovtun, D. T. Son and A. O. Starinets Phys. Rev. Lett. **94**, 111601 (2005) [arXiv:hep-th/0405231].
16. Jean-Yves Ollitrault, Phys. Rev. D **46**, 229-245 (1992).
17. Jean-Yves Ollitrault, private communication.
18. T. Hirano and Y. Nara, Nucl. Phys. A **743**, 305 (2004) [arXiv:nucl-th/0404039].
19. D. Teaney, J. Lauret and E. V. Shuryak, arXiv:nucl-th/0110037. *ibid.*, Phys. Rev. Lett. **86**, 4783 (2001)
20. P. F. Kolb, P. Huovinen, U. W. Heinz and H. Heiselberg, Phys. Lett. B **500**, 232 (2001) [arXiv:hep-ph/0012137].
21. P. Huovinen, P. F. Kolb, U. W. Heinz, P. V. Ruuskanen and S. A. Voloshin, Phys. Lett. B **503**, 58 (2001) [arXiv:hep-ph/0101136].

22. C. Nonaka and S. A. Bass, Phys. Rev. C **75**, 014902 (2007)
23. P. Huovinen and P. V. Ruuskanen, Ann. Rev. Nucl. Part. Sci. **56**, 163 (2006) [arXiv:nucl-th/0605008].
24. P. F. Kolb and U. W. Heinz, arXiv:nucl-th/0305084.
25. R. Baier, P. Romatschke, D. T. Son, A. O. Starinets and M. A. Stephanov, JHEP **0804**, 100 (2008) [arXiv:0712.2451 [hep-th]].
26. M. A. York and G. D. Moore, arXiv:0811.0729 [hep-ph].
27. B. Betz, D. Henkel and D. H. Rischke, arXiv:0812.1440 [nucl-th].
28. S. Bhattacharyya, V. E. Hubeny, S. Minwalla and M. Rangamani, JHEP **0802**, 045 (2008) [arXiv:0712.2456 [hep-th]].
29. P. Huovinen and D. Molnar, Phys. Rev. C **79**, 014906 (2009) [arXiv:0808.0953 [nucl-th]].
30. H. Song and U. W. Heinz, Phys. Rev. C **78**, 024902 (2008) [arXiv:0805.1756 [nucl-th]].
31. M. Luzum and P. Romatschke, Phys. Rev. C **78**, 034915 (2008) [arXiv:0804.4015 [nucl-th]].
32. V. Greco, M. Colonna, M. Di Toro and G. Ferini, arXiv:0811.3170 [hep-ph].
33. Z. Xu and C. Greiner, Phys. Rev. C **71**, 064901 (2005) [arXiv:hep-ph/0406278].
34. C. Gombeaud and J. Y. Ollitrault, Phys. Rev. C **77**, 054904 (2008) [arXiv:nucl-th/0702075].
35. M. L. Miller, K. Reygers, S. J. Sanders and P. Steinberg, Ann. Rev. Nucl. Part. Sci. **57**, 205 (2007) [arXiv:nucl-ex/0701025].
36. P. Steinberg, private communication.
37. see for example, S. A. Voloshin, A. M. Poskanzer and R. Snellings, arXiv:0809.2949 [nucl-ex].
38. R. Snellings, private communication.
39. The data presented are from the thesis Dr. Yuting Bai.
40. see for example, B. I. Abelev *et al.* [STAR Collaboration], Phys. Rev. C **77**, 054901 (2008) [arXiv:0801.3466 [nucl-ex]].
41. H. J. Drescher, A. Dumitru and J. Y. Ollitrault, arXiv:0706.1707 [nucl-th]; in N. Armesto *et al.*, “Heavy Ion Collisions at the LHC - Last Call for Predictions,” J. Phys. G **35**, 054001 (2008).
42. For discussion see, A. Dumitru *et al.*, Phys. Lett. B **460**, 411 (1999).
43. S.S. Shi, for the STAR Collaboration. Presented at Quark Matter 2009.
44. For a recent account see, D. Kharzeev, E. Levin and M. Nardi, arXiv:0707.0811 [hep-ph].
45. D. Kharzeev, E. Levin and M. Nardi, Nucl. Phys. A **730**, 448 (2004) [Erratum-ibid. A **743**, 329 (2004)] [arXiv:hep-ph/0212316].
46. T. Hirano, U. W. Heinz, D. Kharzeev, R. Lacey and Y. Nara, Phys. Lett. B **636**, 299 (2006) [arXiv:nucl-th/0511046].
47. H. J. Drescher, A. Dumitru, A. Hayashigaki and Y. Nara, “The eccentricity in heavy-ion collisions from color glass condensate Phys. Rev. C **74**, 044905 (2006) [arXiv:nucl-th/0605012].
48. T. Lappi and R. Venugopalan, Phys. Rev. C **74**, 054905 (2006) [arXiv:nucl-th/0609021].
49. J. Y. Ollitrault, A. M. Poskanzer and S. A. Voloshin, arXiv:0904.2315 [nucl-ex].
50. R. S. Bhalerao and J. Y. Ollitrault, Phys. Lett. B **641**, 260 (2006) [arXiv:nucl-th/0607009].
51. B. Alver *et al.* [PHOBOS Collaboration], Phys. Rev. Lett. **98**, 242302 (2007) [arXiv:nucl-ex/0610037].
52. M. Miller and R. Snellings, “Eccentricity fluctuations and its possible effect on elliptic

58 *Derek A. Teaney*

- flow arXiv:nucl-ex/0312008.
53. S. A. Voloshin, A. M. Poskanzer, A. Tang and G. Wang, Phys. Lett. B **659**, 537 (2008) [arXiv:0708.0800 [nucl-th]].
 54. B. Alver *et al.*, Phys. Rev. C **77**, 014906 (2008) [arXiv:0711.3724 [nucl-ex]].
 55. A. Bazavov *et al.*, arXiv:0903.4379 [hep-lat].
 56. K. Itakura, O. Morimatsu and H. Otomo, Phys. Rev. D **77**, 014014 (2008) [arXiv:0711.1034 [hep-ph]].
 57. Derek Teaney, Phys. Rev. D **74**, 045025 (2006).
 58. A. J. Kox, S. R. de Groot, and W. A. van Leeuwen, Physica **84A**, 155 (1976).
 59. M. Prakash, M. Prakash, R. Venugopalan and G. Welke, Phys. Rept. **227**, 321 (1993); see also R. Venugopalan, Ph.D. thesis, Stony Brook (1992).
 60. E. Beth and G. E. Uhlenbeck, Physica **4**, 915 (1937).
 61. R. Venugopalan and M. Prakash, Nucl. Phys. A. **546**, 718 (1992).
 62. N. Demir and S. A. Bass, arXiv:0812.2422 [nucl-th].
 63. P. Arnold, G. D. Moore and L. G. Yaffe, JHEP **0305**, 051 (2003) [arXiv:hep-ph/0302165].
 64. G. Baym, H. Monien, C. J. Pethick and D. G. Ravenhall, Phys. Rev. Lett. **64** (1990) 1867.
 65. R. Baier, A. H. Mueller, D. Schiff and D. T. Son, Phys. Lett. B **502**, 51 (2001) [arXiv:hep-ph/0009237].
 66. P. Aurenche, F. Gelis, R. Kobes and H. Zaraket, Phys. Rev. D **58**, 085003 (1998) [arXiv:hep-ph/9804224].
 67. See for example, M. Le Bellac, *Thermal Field Theory* (Cambridge University Press, Cambridge, England, 1996).
 68. H. B. Meyer, arXiv:0809.5202 [hep-lat].
 69. G. Aarts, C. Allton, J. Foley, S. Hands and S. Kim, Phys. Rev. Lett. **99**, 022002 (2007) [arXiv:hep-lat/0703008].
 70. G. Aarts and J. M. Martinez Resco, JHEP **0204**, 053 (2002) [arXiv:hep-ph/0203177].
 71. P. Petreczky and D. Teaney, Phys. Rev. D **73**, 014508 (2006).
 72. see for example, T. Schaefer and D. Teaney, arXiv:0904.3107 [hep-ph].
 73. P. Arnold, C. Dogan and G. D. Moore, Phys. Rev. D **74**, 085021 (2006) [arXiv:hep-ph/0608012].
 74. D. Kharzeev and K. Tuchin, JHEP **0809**, 093 (2008) [arXiv:0705.4280 [hep-ph]].
 75. G. D. Moore and O. Saremi, JHEP **0809**, 015 (2008) [arXiv:0805.4201 [hep-ph]].
 76. K. Huebner, F. Karsch and C. Pica, Phys. Rev. D **78**, 094501 (2008) [arXiv:0808.1127 [hep-lat]].
 77. J. D. Bjorken, Phys. Rev. D **27**, 140 (1983).
 78. G. Baym, Phys. Lett. B **138** (1984) 18.
 79. M. Gyulassy, Y. Pang and B. Zhang, Nucl. Phys. A **626**, 999 (1997) [arXiv:nucl-th/9709025].
 80. see for example, A. Milov [PHENIX Collaboration], J. Phys. Conf. Ser. **5**, 17 (2005) [arXiv:nucl-ex/0409023].
 81. P. F. Kolb, J. Sollfrank, and U. Heinz, Phys. Rev. C **65**, 054909 (2000).
 82. T. Hirano, private communication.
 83. F. Karsch, E. Laermann, P. Petreczky, S. Stickan and I. Wetzorke, Phys. Lett. B **530**, 147 (2002) [arXiv:hep-lat/0110208].
 84. M. Asakawa, T. Hatsuda and Y. Nakahara, Prog. Part. Nucl. Phys. **46**, 459 (2001) [arXiv:hep-lat/0011040].
 85. W. Hiscock, L. Lindblom, Phys. Rev. **D31**, 725 (1985).
 86. W. A. Hiscock and L. Lindblom, Annals Phys. **151**, 466 (1983).

87. L. P. Kadanoff and P. C. Martin, *Ann. Phys.* **24**, 419 (1963).
88. D. Forster, *Hydrodynamics, Fluctuations, Broken Symmetry, and Correlation Functions*, Perseus Books (1990).
89. Lee Lindblom, arXiv:gr-qc:9508058.
90. W. Israel and J. M. Stewart, *Annals Phys.* **118**, 341 (1979).
91. R. Geroch and L. Lindblom, *Phys. Rev. D* **41**, 1855 (1990).
92. D. Pavón, D. Jou and J. Casas-Vásquez, *Ann. Inst. Henri Poincaré, Sect. A* **36**, 79 (1982).
93. H. C. Öttinger, *Physica A* **254** (1998) 433-450.
94. R. Geroch and L. Lindblom, *Annals Phys.* **207**, 394 (1990).
95. W. Israel, *Ann. Phys.* **100** (1976) 310
96. I. Müller, *Z. Phys.* **198**, 329 (1967).
97. M. Natsuume and T. Okamura, *Phys. Rev. D* **77**, 066014 (2008) [Erratum-ibid. *D* **78**, 089902 (2008)] [arXiv:0712.2916 [hep-th]].
98. A. Muronga and D. H. Rischke, arXiv:nucl-th/0407114.
99. Peter Arnold, Guy D. Moore, and Laurence G. Yaffe, *J. High Energy Phys.* **11**, 001 (2000).
100. S. R. De Groot, W. A. Van Leeuwen and C. G. Van Weert, *Relativistic Kinetic Theory. Principles And Applications*, Amsterdam, Netherlands: North-holland (1980).
101. F. Cooper and G. Frye, *Phys. Rev. D* **10**, 186 (1974).
102. E. Braaten and M. H. Thoma, *Phys. Rev. D* **44**, 2625 (1991). *Phys. Rev. D* **44**, 1298 (1991).
103. Guy D. Moore, private communication. See also Ref.²⁶.
104. D. Molnar, private communication.
105. J. Vredevoogd and S. Pratt, arXiv:0810.4325 [nucl-th].
106. P. F. Kolb, U. W. Heinz, P. Huovinen, K. J. Eskola and K. Tuominen, *Nucl. Phys. A* **696**, 197 (2001) [arXiv:hep-ph/0103234].
107. Derek Teaney, *J. Phys. G* **30** S1247-S1250 (2004).
108. M. Martinez and M. Strickland, arXiv:0902.3834 [hep-ph].
109. U. W. Heinz, K. S. Lee and M. J. Rhoades-Brown, *Phys. Rev. Lett.* **58**, 2292 (1987).
110. C. M. Hung and E. V. Shuryak, *Phys. Rev. C* **57**, 1891 (1998) [arXiv:hep-ph/9709264].
111. F. Reif, *Fundamentals of Statistical Physics*, McGraw-Hill (1965).
112. A. El, A. Muronga, Z. Xu and C. Greiner, arXiv:0812.2762 [hep-ph].
113. Z. Xu and C. Greiner, *Phys. Rev. Lett.* **100**, 172301 (2008) [arXiv:0710.5719 [nucl-th]].
114. K. Dusling, private communication.
115. D. Teaney, and K. Dusling, in progress.
116. S. S. Adler *et al.* [PHENIX Collaboration], *Phys. Rev. Lett.* **97**, 052301 (2006) [arXiv:nucl-ex/0507004].
117. B. Alver *et al.* [PHOBOS Collaboration], arXiv:0812.1172 [nucl-ex].
118. B. I. Abelev *et al.* [STAR Collaboration], *Phys. Rev. Lett.* **102**, 052302 (2009) [arXiv:0805.0622 [nucl-ex]].
119. B. I. Abelev *et al.* [STAR Collaboration], *Phys. Rev. Lett.* **98**, 192301 (2007) [arXiv:nucl-ex/0607012].
120. A. Adare *et al.* [PHENIX Collaboration], *Phys. Rev. Lett.* **98**, 172301 (2007) [arXiv:nucl-ex/0611018].